Macrospicules, Jets and the Solar Chromosphere

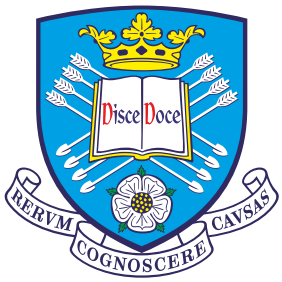

Samuel Middleton Bennett

School of Mathematics and Statistics

The University of Sheffield

This dissertation is submitted for the degree of

Doctor of Philosophy

Supervisor: Robertus Erdélyi

December 2017

To Sue and Steve, thank you for everything.

Acknowledgements

I would like to thank all teachers, lecturers and supervisors who have supported me throughout my education. The faculty of SoMaS have been immensely supportive throughout all problems and successes that have come my way. Most importantly I would like to thank Robertus for his support. He has pushed me to become the very best scientist I could be, and I cannot thank him enough.

I am an immensely annoying person to live with, so I would like to thank Nabil Freij for putting up with my slovenliness for three and a half years. Stuart Mumford, for the Python lessons, particularly during first year, and Drew Leonard for being a rubber duck on all too regular a basis. Thank you to Stevie Chaffin, Alex Hague, Freddie Mather, Chris Nelson and all the solar physics PhD's in the office of doom, for mutual stress in the difficult times and elation in the good. I would also like to thank everyone at the University of Sheffield Cycle Club, there are too many to mention by name, you were an excellent outlet when I needed one.

I would like to thank my family, Sue, Steve and Kathryn for their confidence in me, infinite patience when and for keeping me grounded. Kimberley, thank you for you non-stop belief in me.

Abstract

Given recent advancements in observational solar physics, both in quality and quantity, the time is right to revise the chromospheric feature, macrospicules. These jet-like phenomena are larger than their semi-namesake spicules, which only extend to 10 Mm as an absolute maximum and are ubiquitous in the solar chromosphere, particularly within intergranular lanes. However, macrospicules are not as large as the so-called coronal jets or the X-ray jets, generally observed in hotter temperature lines and penetrating much higher into the solar atmosphere. The aim of this work is to better classify macrospicules as a population and to detect any possible relationships; such as relation to the solar cycle, impacts on coronal heating or as a solar wind accelerator, on a global scale.

This is achieved first by means of a statistical sample of macrospicules. We utilise the first two and a half years of Atmospheric Imaging Assembly on board the Solar Dynamics Observatory's (AIA/SDO) operation window and measure macrospicules properties throughout. This two and a half year sample acts as a proxy for the ramp from solar minima in mid 2010 to maxima in late 2012. Over this time period we find a general increasing trend for the properties of the macrospicules. A range of charcteristic features of the macrospicules, such as: maximum length and width, maximum velocity and lifetime are stated and compared to the current literature. This same sample is then tested against the Carrington longitude to test for any relation to what has been termed, an active longitude. In this case, we find that the macrospicules do have a correlation to the so-called active longitude.

Lastly, this work presents a detailed case study of a macrospicule, utilising a wide range of available imagers. The case study involves a jet-like feature that is seen at the solar limb in Crisp Imaging Spectropolarimeter at the Swedish Solar Telescope, AIA/SDO and the Extreme Ultra Violet Imager on STEREO (Solar Terrestrial Earth RElations Observatory). Applying a Markov Chain Monte Carlo method we analyse the spectroscopic data from CRISP and build a profile of the line of sight velocities of the jet. Lastly, we attempt to determine whether or not the jets have an effect on the atmosphere above it.

Table of contents

Chapter 1

Introduction

1.1 The Sun

The Sun is an extremely complex system, consisting primarily of ionised plasma, the formation of which generated the collection of planets and asteroids we call the solar system. As such, the study of our nearest star should be at the forefront of our research into the cosmos; any model we build to examine other stars must first accurately describe our star. The Sun takes its place on the Hertzsprung-Russell [Hertzsprung (1909); Russell (1914)] diagram as an early life main sequence star at the yellow end of the stellar spectrum. It is a population 1 star, meaning that it has a high metallic content, a fact which aids in our observations immeasurably.

1.1.1 Solar Interior

The structure of the Sun can be divided into internal and external regions. Internal structure has been inferred by the use of techniques such as helioseismology, therefore we still have many questions as to the exact mechanisms dominating below the photosphere. At the centre is the solar core, wherein fusion takes place. Followed by the radiative zone, tachocline and convective zone.

The tachocline has the greatest impact on the solar atmosphere, as it has also been proposed as the source for a dynamo generating the magnetic field. The most important result of the tachocline is that at this point, the motion changes from uniform behaviour of the radiation zone to the differential rotation of the convective zone. This differential rotation is the cause of extremely complex global magnetic field permeating the Sun. The tachocline, as discussed in Brun (2001), is a thin layer between the radiative zone and the convection zone, of which not a great deal is known. A particular impact of the tachocline's existence, is that the $p-mode$ oscilla-

tions used in helioseismology, interact strongly with it, as demonstrated in Chaplin (2014), to the point of filtering high order oscillations out. There have been recent studies, such as Obridko and Shelting (2007), which suggest that the tacholine is responsible for several 1.3 to 3 year cycles in features observed higher in the solar atmosphere, however this has not been definitively proven.

Above the tachocline, there is the onset of convection, naming this region of the solar interior. The convective cells of heating and cooling plasma carry the magnetic field from the tachocline up to the bottom of the photosphere. The tops of these cooling cells, hotter plasma in the centre and cooler, darker, plasma at the edges form the granulation ubiquitous in any image of the photosphere [Åke Nordlund et al. (2009)]. Convective cells are responsible for the transport of magnetic field from the tachocline to the photosphere, hence they have a significant effect on the solar atmosphere's structure.

1.1.2 The solar atmosphere

The photosphere is the minima of the solar temperature profile, with a temperature range starting at 6000 K at the base, and 4700 K at the top. It emits light in the visible band of the electromagnetic spectrum, a property utilised in spectrascopic imaging of the solar atmosphere. The granulation resulting from the convective region appears as dark lines and bright 'bubbles' expanding and collapsing as hot material rises, cools and consequently falls back down into the solar interior, [Åke Nordlund et al. (2009)]. These features tend to measure approximately 2 Mm from one boundary to the other, which, are know as inter-granular lanes.

The most prominent feature in the photosphere are sunspots. These features are significantly cooler that the surrounding photosphere, with a dark centre, known as the umbra, through which open magnetic field emerges from the solar interior. Spreading away from the umbra is the penumbra, a ring of long thin structures spreading away from the umbra. These have been widely studied and have become known as fibrils, which transport waves into the atmosphere from the solar interior [Rouppe van der Voort and de la Cruz Rodríguez (2013)]. Sunspots are normally part of an extremely complex system of magnetic field, meaning that there are usually many in one active region. Sunspots are widely used as indicators of solar activity, the study of them has lead to the discovery of the 11 and 22 year solar cycles. Analysis of their locations has also lead to the proposition of an active longitude, where sunspot formation is more frequent, the testing of this concept with macrospicules is the subject of The photosphere is the coolest point in the solar temperature profile, from this point the temperature of the solar atmosphere

will continue to increase with distance from the photosphere.

The layer above the photosphere, is the chromosphere, so called, as when observed during solar eclipses, it appears colourful. The density drops sharply from the photosphere to the order of 10^{-4} and is approximately 2 Mm thick. Over this 2 Mm layer the temperature rises from 4,700 K to 25,000 K, see *e.g.* Withbroe and Noyes (1977). This result is currently one of the primary focuses of the solar research community. The chromosphere is incredibly complex, particularly with respect to its magnetic structure and the transport of heat, consequently the chromosphere plays an essential role in the formation of explosive events such as solar flares and coronal mass ejections (CMEs).

Prevalent in the chromospheric, and subsequently the coronal spectral lines, are the magnetic field lines which are rooted in the sunspots, demonstrated in Athay and Beckers (1976). These appear as large-scale loops of plasma which has been locked into the magnetic field lines, extending through this region and right into the corona, they regularly reach 10s of Mm into the atmosphere. Lower in the chromosphere, we find a second, smaller-scale population of loops, measuring only a few Mm across. Small-scale chromospheric loops have been presented as a possible link between the photosphere and the chromosphere, due the their most likely formation being a small-scale flux emergence event [Ulmschneider and Stein (1982)].

Particularly noticeable in the chromosphere are the footprints of the coronal holes [Cranmer (2009)]. These appear as regions of dark amongst the bright chromospheric features, this is a result of the cool plasma, lower in the atmosphere becoming visible through these holes. During the minimum phase of the solar cycle, there are usually two prominent coronal holes at the solar poles. These can cover half of the solar disk during particularly inactive solar minima, however, at solar maxima, these polar coronal holes disappear as the magnetic field becomes increasingly complex. The coronal holes are characterised by magnetic field lines extending up though the solar atmosphere, whereas, in the quiet Sun (areas not coronal holes) the magnetic field lines are closed, generally forming small and large scale loops.

At the top of the chromosphere, the temperature of the plasma increases rapidly over a very short distance, approximately 500 km. This is known at the transition region, [Mariska (1986)]. It acts as a barrier, and amplifier, between the chromosphere and corona with the temperature rising from 25,000 K to 1 MK. The mechanism which causes this is still not understood and is one of the prominent problems in solar physics.

Above the transition region we find the corona, Golub and Pasachoff (2009), high temperature plasma whose behaviour is now dominated by the magnetic field

emerging from the solar interior. We can tell that Iron is ionised from observations, therefore, the coronal temperature has a minimum value of 1×10^6 K. The corona is a complex system where exceptionally large scale features can have far reaching effects on the solar environment, [Reale (2014)] *e.g.* coronal loops, streamers and transient events such as CME's and solar flares. Coronal loops, CME's and solar flares are tightly related, solar flares regularly form as a result of sunspot, and therefore coronal loop, migration towards the equator. As the sunspots migrate, the magnetic tension of the loop increases to the point at which a reconnection event is the only way of reducing the magnetic energy in the system. Solar flares are the direct result of this reconnection in violent bursts producing EM radiation in X-Ray The material in the overlying loops becomes unbound as a result of the release of magnetic tension, and is released in the form of a CME, although this is not always the case. The material ejected both in solar flares and CME's will then either fall back to the solar surface as coronal rain, or, will integrate into the solar wind.

1.1.3 Observations

History

Study of the Sun took a large step forward when observatories such as the Royal Greenwich Observatory began taking measurements in 1874. Now with consistent imaging from the same source and a history of smaller observations combined, larger patterns within sunspots was revealed. Taking a monthly average of the sunspot count revealed a rise and fall in the sunspot number count over an 11 period, now referred to as the solar 11-year cycle. Sunspot numbers in modern times are calculated by the number of sunspot groups multiplied by 10 as that is the average number of sunspots in a sunspot group. This definition is utilised by the National Oceanic and Atmospheric Administration (NOAA) in America and Solar Influences Data Analysis Centre in Belgium (SIDC) in Belgium. Both of these organisations monitor the Sun and its impact on Earth including radio flux and total solar irradiance. All of these can be used as a proxy to demonstrate the 11-year solar cycle.

If we plot the date of the sunspots occurrence with respect to their latitude, we produce another diagram demonstrating the 11-year cycle. This is the now famous butterfly diagram in which populations of sunspots tend to form closer and closer to the equator before a break point at which they begin forming further away, the time scale of which is 11 years.

This is a result of the differential rotation mechanism in action in the Sun's motion. As the magnetic field becomes increasingly complex and the bands of magnetic polarity grow closer, increasingly more sunspots are pushed to the solar equa-

tor. This demonstrates that the 11-year cycle is result of the magnetic field and dynamo. The Debrecen Photoheliographic Data (DPD) sunspot catalogue continued the work of the Greenwich catalogue, recording sunspot groups location and size. This catalogue forms the basis for the analysis of the macrospicules with respect to the Carrington rotation presented in Chapter 4.

Observational Solar Spectroscopy

Newton was the first to observe that light from the Sun could be divided into its component parts using a simple prism, but it was a very long time before we would reach a point where this information could be used for science. Spectroscopy now forms the basis for almost all solar observations, the numerous heavy elements present in the Sun's atmosphere mean that it is extremely effective over range of temperatures.

Figure 1.1 demonstrates the white light solar spectrum, immediately apparent are the dark absorption lines. They are a result of the quantum mechanical effects of the electron energy shells around atoms and molecules. In the case of the Sun, a continuous spectrum is radiated from the photosphere and this light then interacts with the elements higher up in the atmosphere. Upon collision with an atom or molecule, the exact wavelength of light which corresponds to the energy required to excite an electron from one energy level to another is absorbed by that electron. The direct result of this is that the wavelength absorbed in the energy transaction is absent from the white-light spectrum being emitted from the photosphere, and hence appears as a dark line when observed from beyond the solar atmosphere. These transition lines are closely aligned to the temperature at which they are formed.

In the case of Hydrogen, the most prevalent atom in the Sun, the array of lines generated by the transitions between energy shells is known as the Balmer series. The primary line in this range is Hα, which, is widely used in solar observations as it covers the photosphere and lower chromosphere. The complexity is that the line is broad, for example, the Hα CRISP filter at the SST (see Section 1.1.4) can measure $\pm$2 nm about the main emission line 656.28 nm. This allows complex analysis of solar features, but the data must be handled carefully, environmental factors such as magnetic field and temperature can alter the emission line. Chapter 5 utilises the extremely detailed images provided by CRISP to calculate dopplergrams of a jet-like feature at the solar limb.

The emission lines correspond to the ionisation temperature of the particular ion, therefore, one atom can form multiple emission lines at a range of temperatures as different ions form. As a result of this, Fe VIII (13.1 nm), Fe IX (17.1 nm), Fe XII

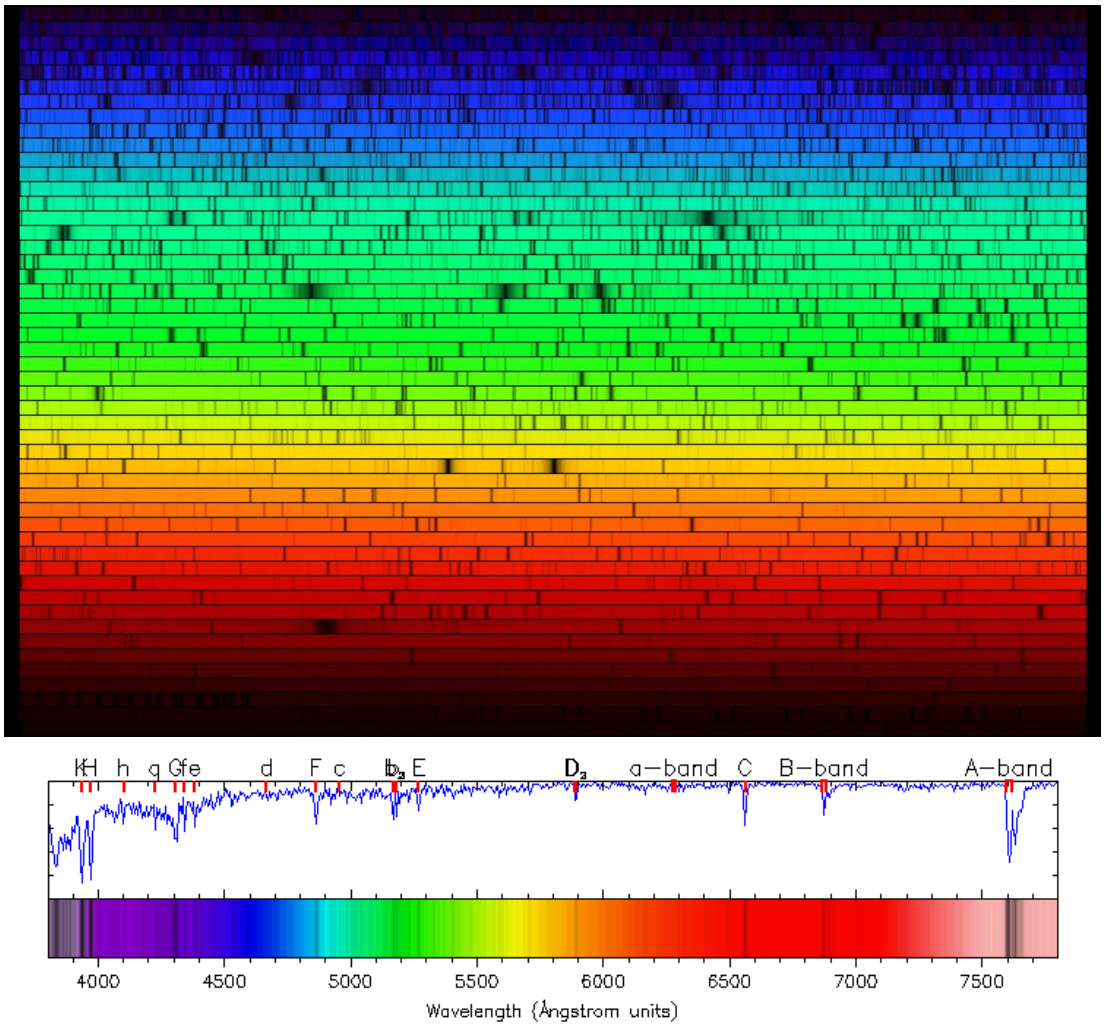

Fig. 1.1 The top figure is a visible light measurement of the Sun. It demonstrates that there are elements in the atmosphere absorb the light and appears on this spectrum as a dark line. The Fraunhofer lines (absorption lines) are marked on a continuous spectrum with an intensity profile below. http://media.radiosai.org/journals/Vol_05/01JAN07/04-musings.htm

(19.3 nm), Fe XIV (21.1 nm), Fe XVI (33.5 nm) and Fe XVIII (9.4 nm) are all observed by the spacecraft Solar Dynamic Observatory (SDO) with the Atmospheric Imaging Assembly (AIA), Schmelz et al. (2013).

Having presented the principles with which we observe the solar atmosphere, we now need a base to image the Sun from.

1.1.4 Observational Platforms

In the current solar observation climate, we have a wealth of information, coming from many different sources. Understanding the functionality of these instruments in terms of the raw method is essential to rigorous science and accurate readings.

Ground-Based Telescopes

Solar physics spent its early development being applied in ground-based solar telescopes, as has already been discussed, particularly in centres such as Royal Greenwich Observatory and Meudon Observatory in Paris. In the modern era, the most powerful instruments, delivering high cadence and spatial resolution, are based on the ground..

On La Palma in the Canary Islands, at 2360 m altitude, the Swedish Solar Telescope is situated. The SST utilises two optical pipelines, one for the red end of the electromagnetic spectrum and another examining the blue end. The CRisp Imaging SpectroPolarimeter (CRISP), focuses on the red end of the visible spectrum, whereas the soon to be updated instrument, Chromis, analyses the blue end. The beam is split upon its arrival at the optical bench and sent to either of these instruments, but before the beam reaches CRISP there is a layer of correction known as adaptive optics.

As a result of the above points, the images from the SST are extremely customisable. They are usually returned as data cubes, the dimensions of which are time, wavelength, x and y. The resolution of these features are therefore changeable dependant on the requirements of the observation. Cadence can be as low as 2.5 s, the spectral increment, 0.02 nm, and spatial resolution of 0.12 arcsec. Given the impressive results produced by these facilities, an ambitious new telescope is being built in Hawai'i, the Daniel K. Inouye Solar telescope (DKIST). DKIST promises to be the most powerful solar telescope ever created with a 4 m mirror, enabling resolution of 10 km per pixel and overcoming the current quantity of photons issues at the limb for spectropolarimetry.

Space Based Telescopes

Space borne telescopes have a significant advantage over their ground based counterparts due to the nearly constant un-interrupted, view of the Sun without the atmospheric effects disturbing the signal. As a result, the volume of space based instrumentation has grown exponentially since the early Skylab missions taking solar images from a low Earth orbit.

The first solar mission to move on from imagers on space stations was the Solar Heliospheric Observatory (SoHO). Placed at the gravitationally stable Lagrange point, L1, between the Sun and Earth, it affords constant viewing of the Sun. The mission marks a sea change in solar observations. The range of instruments on board covered the entire solar atmosphere, [St. Cyr et al. (1995)], and our understanding of the Sun has been continually updated by its findings. Originally, it was designated as a two year mission, however the mission continues to be a success and has been running for 2 decades [Fleck et al. (2006), Fleck and Müller (2016)] The primary scientific goals were examining photospheric behaviour, EUV imaging of the chromosphere and investigation of impactful solar weather using LASCO.

The Japanese Aerospace Exploration Agency (JAXA) have organised several solar missions. Solar-A, renamed Yohkoh, Tsuneta et al. (1991) upon its successful launch and commencement of observations, pre-dates SoHO. It covered soft and hard X-Ray ranges and spectrometers covering, specifically, the coronal iron lines and a wide band spectrometer. Yohkoh was particularly successful with respect to the detection of high energy events, and was used for Shibata's studies of X-Ray jets and their formation mechanisms. The work undertaken by Shibata provides an excellent example for the study in Chapter 3.

JAXA's next mission was Hinode signified a significant move forward in space based solar observations, building from what was successful in Yohkoh. The mission introduced small wavelength increment spectroscopy to space based missions. The EUV Imaging Spectrometer (EIS) is designed to examine the chromosphere using two specific imaging techniques. It is extremely flexible with 4 slit or slot positions, 1" pixel slit, 2" pixel slit, 40" pixel slot and 266" and two different modes for spectroscopy.

Possibly the most adventurous mission to probe the solar environment to date, is the STEREO mission (Solar TErrestrial RElations Observatory) described in Kaiser et al. (2008). As is suggested by the name of this mission, the primary focus was to form a more comprehensive picture of the solar atmosphere, by positioning two satellites in such an orientation to build a three dimensional picture. Consequently, two identical satellites were launched into orbit, ahead of and behind the Earth.

There is an inherent differential in the angular velocity of the spacecraft, in order to move the spacecraft ever further around the orbit at approximately 45° per year. The primary objective of this stage of the mission was to obtain the optimal angle to produce three dimensional images of the Sun using a tomographic technique.

Given that STEREO was designed to give varying angles of the Sun-Earth environment, the instruments on the mission are tailored to this need. SECCHI is a suite of 5 imagers, utilising white-light coronographs, an extreme ultra violet imager and two wide angle Heliospheic Imagers (HI) designed to track CMEs to 1 AU. STEREO's positioning is advantageous to this work as it affords a different viewing angle on features. This can come in useful when considering features at the limb. If STEREO is positioned correctly, it aids in reducing uncertainty when considering possible line of sight effects.

Building on all of the above missions, the Solar Dynamics Observatory (SDO) mission began in 2010, proposed in Pesnell et al. (2012). The instruments are developments of concepts used on previous missions but expanding them to allow constant viewing of the entire solar disk. Consequently all instruments on SDO view the full solar disk, at all times, maintaining the same temporal cadence. Therefore, the SDO mission produces significantly more raw data than any previous missions. From a purely engineering standpoint, the instruments were carefully selected to facilitate the downloading of the data. As such, SDO has three instruments; the Helioseismic and Magnetic Imager (HMI); the Extreme Ultraviolet Variability Experiment (EVE) and the Atmospheric Imaging Assembly (AIA) investigating the upper chromosphere and corona.

AIA's imaging suite provides full disk images in 4096 × 4096 resolution and most importantly at 12 second cadence. However, its distinguishing feature is the array of wavelengths analysing the atmosphere Lemen et al. (2012) associated with various temperatures corresponding to the appropriate electron transitions. The instrument ranges through 170, 30.4, 160, 17.1, 19.3, 21.1, 33.5, 9.4 and 13.1 nm providing a temperature range of 5000 K to 1.6×10^7 K.

Without SDO the work in this thesis would not be possible. The constant full disk viewing greatly increases the chances of capturing the total evolution of a macrospicule. As such, it is used extensively in all of these studies as the main observational tool in Chapter 3, Chapter 4, and plays an essential role in Chapter 5

1.2 Plasma behaviour

Stars are incredibly complex features despite their apparent simplicity when viewed by the naked eye. Their behaviour is entirely unlike any planetary body, and as

has already been discussed, their inherent magnetic field makes their structure extremely complex. All of these affects can be traced back to the fact that the Sun consists of gas kept at high temperature and pressure, which causes it to form the 4^{th} state of matter, plasma. Plasma is defined as a gas in which the molecules reached an energy level that cause them to eject their outermost electrons and become ions, causing the gas to be a neutral mixture of charged ions and free electrons (produced from ionising the molecules). It can be formed in several situations on Earth, such as a discharge of current from the atmosphere to the ground, manifesting as lightning as the propagating current ionises the air. Plasma dynamics are significantly more complicated than those of a gas, due to the presence of inherent magnetic field. We therefore need a set of laws to define how the plasma behaves on scales such as those applicable on the Sun and in the atmosphere.

1.2.1 Magnetohydrodynamics

Magnetohydrodynamics are the set of laws by which we describe the motion of plasma on large scales. They were derived by Alfvén (1942), an achievement for which, Alfvén was awarded the Nobel Prize. The rules set up are a combination of the gas pressure equations and Maxwell's laws of electrodynamics, so let us now examine this relationship.

When considering a plasma, it is important to remember that while the total charge of the plasma will be quasi-neutral, the ions and electrons which constitute the mixture still carry charge. Consequently, motions in the plasma will cause the charges to have a change in velocity. In accordance with Faraday's law, a moving charge will cause a magnetic field to be induced and Ohms' law will also become a factor with charges moving through a magnetic field. Additionally, the particles which constitute the plasma are gaseous, therefore, their motion can also be described in terms of classical fluid dynamics. As such, this can be an extremely complex problem, let us first consider the Maxwell and gas dynamics equations.

$$\nabla \times \mathbf{E} = -\frac{\partial \mathbf{B}}{\partial t} \quad \text{Faradays Law} \quad (1.1)$$

$$\nabla \times \mathbf{B} = \mu_0 \mathbf{j} + \frac{1}{c^2}\frac{\partial \mathbf{E}}{\partial t} \quad \text{Ampére Law} \quad (1.2)$$

$$\nabla \cdot \mathbf{E} = \frac{\tau}{\epsilon_0} \quad \text{Gauss' Law} \quad (1.3)$$

$$\nabla \cdot \mathbf{B} = 0 \quad \text{Gauss' law of magnetism} \quad (1.4)$$

$$0 = \frac{\partial \rho}{\partial t} + \nabla \cdot (\rho \mathbf{v}) \quad \text{Equation of mass conservation} \quad (1.5)$$

$$0 = \frac{\partial p}{\partial t} + \mathbf{v} \cdot \nabla p + \gamma p \nabla \cdot \mathbf{v} \quad \text{Conservation of entropy} \quad (1.6)$$

where $\mathbf{E}$ is the electric field strength, $\mathbf{B}$ the magnetic field, t is time, $c^2 = (\epsilon_0 \mu_0)^{-1}$,$\epsilon_0$ is the vacuum permittivity, μ_0 is the permeability of free space, $\mathbf{j}$ is the current density and τ is the charge density.

Combining the equations above using the velocity vector, $\mathbf{v}(\mathbf{r}, t)$, and the equation of motion for a fluid element, leads to the basic equations of ideal magnetohydrodynamics (MHD):

$$\frac{\partial \rho}{\partial t} + \nabla \cdot (\rho \mathbf{v}) = 0 \quad (1.7)$$

$$\rho\left(\frac{\partial \mathbf{v}}{\partial t} + \mathbf{v} \cdot \nabla \mathbf{v}\right) + \nabla p - \rho \mathbf{g} - \frac{1}{\mu_0}(\bigtriangledown \times \mathbf{B}) \times \mathbf{B} = 0 \quad (1.8)$$

$$\frac{\partial p}{\partial t} + \mathbf{v} \cdot \nabla p + \gamma p \nabla \cdot \mathbf{v} = 0 \quad (1.9)$$

$$\frac{\partial \mathbf{B}}{\partial t} - \bigtriangledown \times (\mathbf{v} \times \mathbf{B}) = 0 \quad (1.10)$$

$$\nabla \cdot \mathbf{B} = 0 \quad (1.11)$$

These equations are therefore applicable to the case where; 1) the plasma is strongly collisional, such that the time-scale of the collision between the particles is much smaller that the characteristic time scales of the entire system. 2) The resistivity of these collisions is small *i.e.* the magnetic diffusion time scale must be longer than any other process occurring within the plasma. 3) The time-scale must be greater than that of the kinetic processes occurring within the plasma, such as ion gyration, Landau damping and length-scales longer than the ion skin depth and Larmor radius, Goedbloed and Poedts (2004).

By making choices with respect to the units for length, mass and time, the MHD equations can be made dimensionless. A typical length scale can be chosen such as

l_0 to be something sensible and ρ_0 and B_0 are chosen from a representative point in the plasma and the time unit can be inferred from a basic speed of the plasma, *e.g.* the sound speed or Alfvén speed.

$$v_0 \equiv v_{A,0} \equiv \frac{B_0}{\sqrt{\mu_0 \rho_0}} \text{which leads to} t_0 \equiv \frac{l_0}{v_0} \tag{1.12}$$

The density, velocity, magnetic field etc. are then used to define new dimensionless parameters and substituted back into the MHD equations, which remain unchanged but now a have an operator for these variables instead of the variable themselves. The crucial outcome here is that the equations are not dependent on the size of the plasma evaluated, the magnetic field strength, the density or the time scale. After scaling l_0, B_0 and t_0, the pressure term becomes of vital importance and is linked to the ratio between the kinetic pressure of the plasma and magnetic pressure. This ratio is commonly referred to as the plasma beta, which is defined as:

$$\beta \equiv \frac{2\mu_0 p_0}{B_0^2} \tag{1.13}$$

This is and extremely useful flag when considering the behaviour of a plasma at a less precise level, as it indicates the forces dominant in a region. If $\beta \gg 1$ the kinetic pressure terms are dominant, meaning that the kinetic motions of the plasma will determine its overall behaviour, such as in the photosphere and below. Whereas, in the chromosphere and upwards, the balance more favours the magnetic field and the gas movement is determined by magnetic effects.

1.2.2 Reconnection

The above processes are considered to be ideal cases for energy emission. However, in the reconnection process the frozen in condition is violated, as two plasma blobs which were connected by a field line, will now no longer be. This means that the reconnection mechanism itself is non-ideal. In such processes, the magnetic energy is converted to kinetic energy and heat, more on which later.

In order for us to build a model for a reconnective event, several components are required, the magnetic field equations that describe the null point and a description of the current flowing over the change in magnetic field.

In a solar situation, the field lines are hyperbolic, bending away from the centre, forming an X-type neutral point. The limiting field lines are defined in terms of their angle of separation between the hyperboles. The $\bar{\alpha}$ value, which defines the angle between said separatrices, is related to the current density. Which we can calculate

by taking the curl of the magnetic field, Priest and Forbes (2007)

$$\mathbf{j} = -\frac{B_0}{\mu_0 L_0}(1-\bar{\alpha}^2)\hat{\mathbf{z}} \tag{1.14}$$

Where $\hat{\mathbf{z}}$ points out of the xy plane. Now we have reached the point where the current density can be discussed with respect to the null point.

The current sheet typically appears at neutral points where there is a tangential discontinuity, in which case the the magnetic field is tangential and the plasma flow across the current sheet is zero. When the system is in equilibrium, the plasma either side of the sheet, and in the sheet itself, are in pressure balance. Usually, the total magnetic field on the current sheet will be zero, and we assume that the ambient pressures vanish, we can say that the magnetic pressure either side of the sheet is equal to the gas pressure on it:

$$\frac{B_2^2}{2\mu} = p_c = \frac{B_1^2}{2\mu} \tag{1.15}$$

where B_1 and B_2 are the magnetic fields either side of the current sheet and p_c is the gas pressure at the current sheet. It follows that the magnetic field undergoes an exact reversal in the magnetic field. If it is the case that the magnetic field within the sheet is parallel to the y axis and varies in x, is defined $\mathbf{B} = B_y(x)\hat{\mathbf{y}}$, applying Amp'ere's law can give us the current density in z:

$$j_z = \frac{1}{\mu}\frac{dB_y}{dx} \tag{1.16}$$

This means that when we get a steep gradient in B_y with respect to x, a strong current along the current sheet is produced perpendicular to the field lines. This is the current sheet that lies at the heart of reconnection models, however the tangential discontinuity is susceptible to instabilities. Now that we have the null point between the two magnetic fields and the current sheet that forms as a result, we have the environment necessary to begin the reconnection of magnetic field lines.

Let us consider the induction equation again defining how the magnetic field changes with respect to the magnetic field,

$$\frac{\partial \mathbf{B}}{\partial t} = \nabla \times (\mathbf{v} \times \mathbf{B}) + \eta \nabla^2 \mathbf{B} \tag{1.17}$$

with the first term representing the advection and the second the diffusivity of the magnetic field. The ratio of these two terms can be represented by the magnetic Reynolds number, $\Re_m = LV/\lambda$, and of course, this value will dictate the evolution of the induction. The diffusion term dominates in the case where $\Re_m \ll 1$, however,

we must be aware that this condition will not apply on large scales in the solar atmosphere, although it may be true on very small scales. The second mechanism for the changing of the magnetic field lines is advection. Under the condition $\Re_m \gg 1$, we drop the diffusive term from the induction equation.

In Chapter 2 I will examine the current literature with the plethora of solar jets through the solar atmosphere. Chapter 3 will present a statistical study of macrospicules. Chapter 4 investigates the link between macrospicule formation and the Carrington rotation. Chapter 5 presents a case study of a macrospicule like event at the solar limb using simultaneous observations from a range of solar imagers. Lastly I will make my concluding remarks, summarising macrospicules current place in the range of solar ejecta and where the field can progress from here.

Chapter 2

Jets and Macrospicules

The appearance of thin, explosive features with a relatively short lifespan has for a long time, been a part of solar physics. Extremely numerous, explosive and thin jets, were first observed in 1877 by a Vatican observer, Angelo Secchi [Lang (2009)], now dubbed Spicules. This was aided by their sheer ubiquity, they were distinctly visible at the solar limb nearly all the time. However the larger-scale, more infrequent jets were more difficult to observe, particularly with early techniques.

2.0.1 Spicules

Jets and jet-like features are observed throughout the solar atmosphere, and as such a review of the topic is in order. As has already been discussed, spicules are among the smallest jets formed in the solar atmosphere. Most easily observed at the limb, they are long thin structures appearing brightly at the solar limb [Beckers (1972)]. Spicules are found in the chromosphere, regularly observed in the Hα, He II 30.4 nm, Ca II and Si IV [Sterling (2000), Tsiropoula et al. (2012)]. Work by De Pontieu et al. (2007b) divided spicules into two populations, Type-1 and Type-2, with Type-1 being long lived while Type-2 have distinctly shorter lifetimes but are significantly more explosive and grow to much longer lengths. Type-1 spicules have an uprising speed of approximately 20 km s^{-1} and extend to 1 Mm in height with lifetimes of 10 mins, whereas the Type-2 spicules have been shown to extend approximately 5 Mm into the atmosphere and last for an average of 1-2 mins. The most comprehensive difference between the two is in the overall evolution of the feature. Type-1 spicules are observed to have a parabolic evolution, *i.e.* their tip traces out a ballistic arc when plotted against time. Conversely, Type-2 spicules are observed to dissipate or vanish as they evolve, and are primarily observed in the quiet Sun and coronal holes. Type-1 develop in active regions, and as such, Type-2 are far more numerous when recorded in a study such as Pereira et al. (2012).

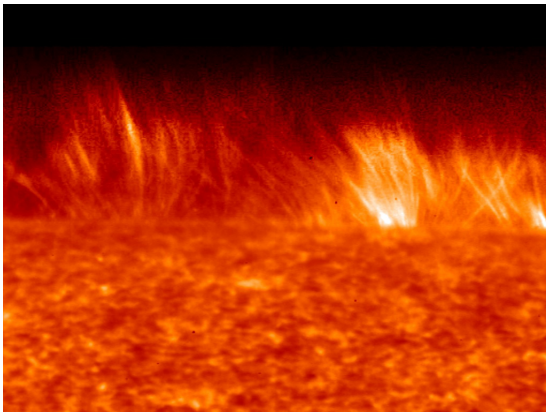

Fig. 2.1 Spicules as observed by at the solar limb using the new IRIS instrument observing at transition region temperatures. http://www.nasa.gov/sites/default/files/images/751917main_highres4_full.jpg

Spicules are visible on the disk as well, but here they are seen as dark thin structures against the bright lower chromosphere. These were initially named mottles and fibrils, but have since been inherently linked with spicules [De Pontieu et al. (2007a); Rouppe van der Voort et al. (2009)].

Since these initial propositions, however, there has been doubt cast as to whether this is indeed the case. Zhang et al. (2012) found no statistical separation of populations within spicules. However, Pereira et al. (2014) have presented evidence that Type-2 spicules disappear from Ca II and reappear in the hotter Si IV and Mg II lines. There is also the proposal that these Type-2 features are Rapid Blue Extensions (RBE's and later Rapid Red Extensions (RRE's)) [Kuridze et al. (2015); Rouppe van der Voort et al. (2015)] This would imply that spicules are heating as they accelerate through the atmosphere. Whether this is because the underlying formation mechanism is different or because there is sufficient energy in the creation of the spicules to cause heating as they propagate through the atmosphere, has yet to be made clear.

The formation of spicules is still a matter of much debate given our currently limited ability to examine small scales in current observations. However, when observations are unable to provide explicit results, numerical and analytic approaches are utilised to fill in the gaps. De Pontieu et al. (2004) outline a mechanism for the formation of spicules which originates in the photosphere based on an anaytic model. *P*-mode oscillations cannot pass through the photosphere due to the minima in the global temperature. However, leakage can occur in specific circumstances, allowing energy to transfer through this gap, until temperatures become high enough to allow propagation to start again. Essential to this model is the inclination of the background magnetic field. The authors report that an inclined field vastly

increases the cut-off frequency of waves tunnelling through the atmosphere. The lower density in the upper solar atmosphere causes the photospheric velocity generated by the *p*-modes to steepen into shocks, which leave an oscillating wake in the chromosphere, the spicule.

However, there are currently two competing theories, wave-driven, as highlighted above and magnetic reconnection. Takeuchi and Shibata (2001) demonstrate a magnetic reconnection model driving formation of spicules, whereas Martínez-Sykora et al. (2011) formed a 3 dimensional model utilising the Lorentz force to push plasma across the solar surface until it meets vertical magnetic field which forces the plasma upwards. Hollweg (1982) demonstrate that a quasi-impulsive source in the photosphere is capable of generating a chain of rebound shocks in the chromosphere, causing the formation of a spicule. Sterling (2000) presents four possible scenarios for the formation of spicules. Three of which utilise a pressure pulse in the photosphere or low chromosphere and higher in the chromosphere. In the simple case, a perturbation at the base of a flux tube, then steepens into a gas-dynamic shock, which is driven higher into the atmosphere upon interaction with the transition region. Lastly, Sterling (2000) describes low and high frequency Alfvén waves, *i.e.* axisymmetric twists on the vertical flux tube in the azimuthal direction. This twisting of the magnetic field then leads to a shock forming the spire of the spicule.

A particularly pertinent model is proposed by Moore et al. (2011), in which magnetic reconnection is instigated by granule-sized 'magnetic bubbles'. As spicules are generally observed to form on the intergranular lanes, this model is particularly pertinent. The authors propose that Type-2 spicules are an analogue for X-Ray jets (Section 2.1.2). In this scenario, magnetic bipoles emerge from the photosphere which then interacts with the ambient field of the lower chromosphere, forming a raft of reconnection external to the bipole.

The advantages of this magnetic field configuration, is that it is extremely common in the solar atmosphere. Additionally, as a result of reconnection between the canopy region which forms over the granules and the more open magnetic fields higher in the atmosphere, shocks and waves are formed, which propagate upwards. The dissipation of the energy within these disturbances has been proposed on numerous occasions to be the central source coronal heading [Athay (2000); Klimchuk (2012); Kudoh and Shibata (1999)].

What becomes evident, after all of these models are formed, is that none of them generate both Type-1, and Type-2 spicules. It is therefore likely that they are indeed two separate features with the model by De Pontieu et al. (2004) forming Type-1 spicules and a reconnection model like that of Moore et al. (2011) is responsible for Type-2.

2.1 Macrospicules

Macrospicules are the focus of this thesis. While these are not as ubiquitous as the smaller namesake, their greater extension, combined with a higher population than the larger jet like features (details to follow), their impact could be greater. Jet-like features have been proposed as the source of solar wind generation, and coronal heating. Macrospicules, with their higher proliferation throughout the chromosphere, have the potential to significantly impact higher solar atmospheres characteristics. Whether this is a direct result of their interaction with the corona or that their formation releases large amounts of excess energy, their properties are worthy of a detailed study.

Therefore, the first topic to be addressed is how are macrospicules different from regular spicules? While spicules are extremely prevalent in any chromospheric images you care to take, macrospicules are significantly rarer. They extend further into the atmosphere, are longer lived that their smaller namesakes and are not dissimilar to jets. However they have been distinguished from the population of jets in the current literature, which will now be discussed below.

Macrospicules were first reported by Bohlin et al. (1975), utilising the SkyLab mission. This was undertaken using the 30.4 nm imager, which took observations of the polar coronal holes. The authors found that the newly named macrospicule was visible in He II 30.4 nm, but was not apparent in Ne VII 46.5 nm or Mg IX 36.8 nm, observing the transition region and corona respectively. They then classified macrospuicules according to 3 observables: that the macrospicules are confined to the coronal holes; that the macrospicules are increasingly inclined away from the normal proportionally to their distance from the solar pole (the authors link this to the supposedly weak, inclined magnetic field again); and lastly that they are only visible in 30.4 nm.

Bohlin et al. (1975) specifically differentiate between macrospicules and the Hα macrospicules previously observed, stating that these new features have no counterpart in that line, citing Moe et al. (1975), who were unable to find a correlation between the two lines by direct observation or numerical correlation. Having said this, they make the caveat that there is a possibility that the formations of the two features could be largely similar.

With the limitations of the observations at that time, there was much debate as to whether this was actually the case. Following up on the work by Bohlin et al. (1975), Labonte (1979) utilised the Big Bear Solar Observatory to examine the 'limb surges' in Hα and Deuterium 3 (D_3). The authors found that the macrospicules in Hα had considerable complexity in their structure, with 'knots, twists and loops'

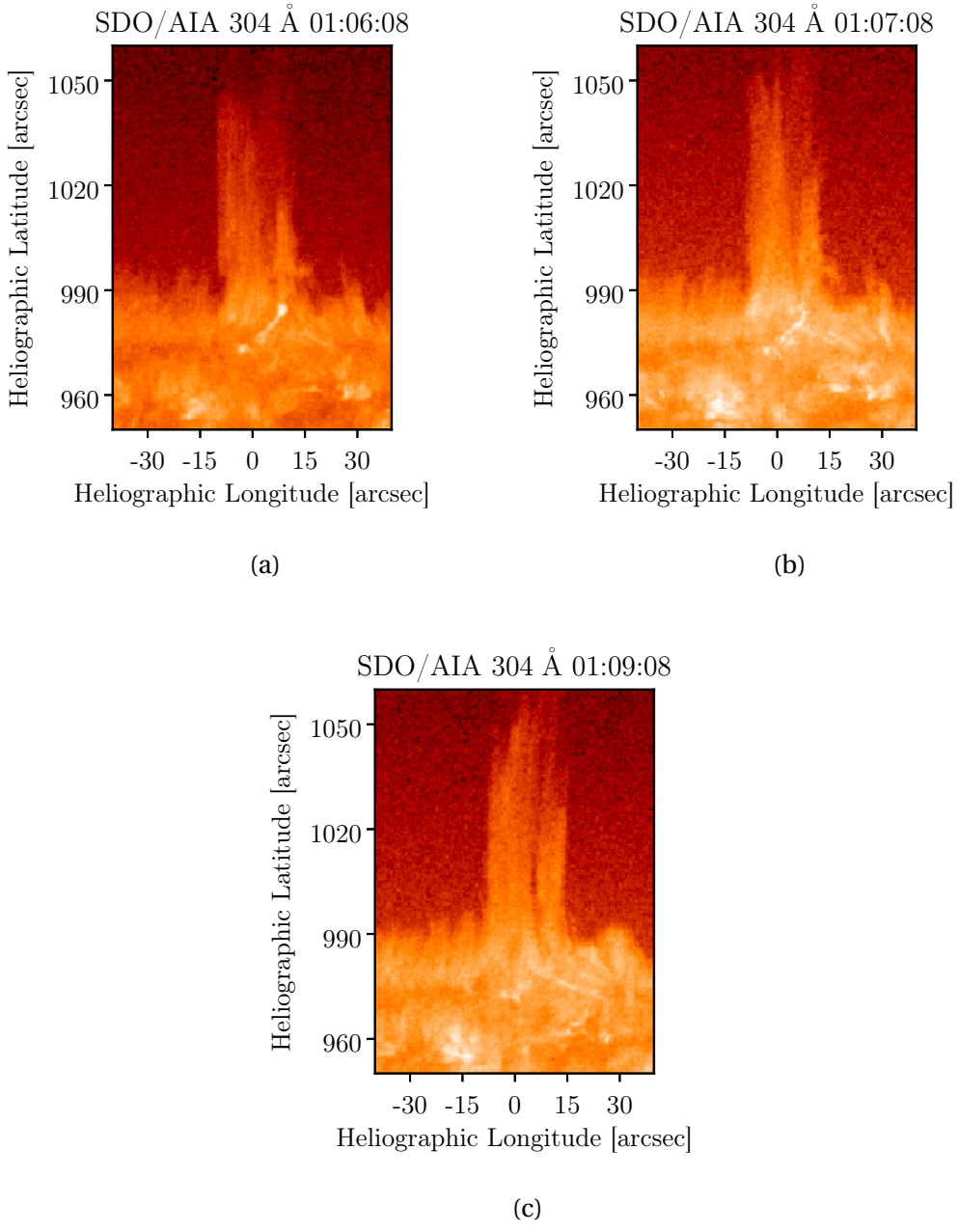

Fig. 2.2 The macrospicule examined by Kayshap et al. (2013). Utilising the 30.4 nm imager on AIA, the authors closely examine the bright point at the base of the jet.

within the confines of the feature. But in D_3, the authors only observe the brightest parts of the macrospicule, usually at the base of the structure apparent in Hα. Differently in this case, the authors also observe features on the disk and define three categories: the macrospicules appearing similar to filament eruptions, surge-like macrospicules and a flare brightening type. Lastly, the paper finds the rate of occurrence of macrospicules to be of the order 1400 per solar day. This discussion as to the possible links between the two features goes on to this day, more on which later.

The next milestone work on macrospicules was published in Dere et al. (1989), again using an early space station, SpaceLab 2, as the platform for space based observations. In this case a Gregorian telescope was used to take a series of broadband UV observations at the solar limb. As a result of this setup the images are a convolution of the intensities from the solar continuum and therefore differentiating between structures is not possible. This means that only macrospicules' spatial extents could be observed, and specifically those which appeared above the limb, with no study of their onset. Consequently, this study was statistical in its focus with the aim of being to ascertain the basic spatial properties of the population.

Dere et al. (1989) then go on to compare the values obtained in this study to the two previously mentioned. The papers are generally in agreement, specifically Dere and LaBonte, citing lengths ranging between 3.75 - 24.75 Mm and similar widths, although Dere et al. find 0.45 - 6.75 Mm and LaBonte 0.45 - 4.5. Mm. The question of velocities is also raised, with values quoted as 20 - 50 km s^{-1} from Dere et al. and $\leq$ 60 km s^{-1} from Labonte (1979). These values should possibly be taken with a pinch of salt as the temporal resolution for Dere and LaBonte was 20 or 60 s and 60 s respectively, which will greatly influence the measurement of the velocity. However, Bohlin et al. (1975). found more extreme values than all of the other studies. Some of the lengths they find extend as far as 45 Mm. They also find greater widths - 3.75-11.25 Mm - and velocities reaching 150 km s^{-1}, although again the temporal resolution is poor, $\geq\sim$ 180 s. Although this early work had its limitations, the groundwork was laid here in order to be more precise when more sophisticated missions would be undertaken in the mid 90s with more focus on detail and less on statistical properties.

With the launch of SoHO in 1996, the community now had continuous viewing of the solar disk, meaning that consistent observations of macrospicules are now possible. On of the first studies utilising the new instruments was undertaken by Pike and Harrison (1997) using the Coronal Diagnostic Spectrometer (CDS). In this case, the instrument scanned from north to south pole, using a mosaic of rastered images, using the He I 58.433 nm, O V 62.973 nm and Mg IX 36.806 lines, corresponding to temperatures of 20,000, 250,000 and 1,000,000 K. In these observations

the macrospicule is apparent at the limb, demonstrating two brightpoints visible in the footpoints either side of the structure, and a fainter column of plasma extending off the limb. Pike and Harrison (1997) find that the macrospicule is visible in the He I and O V lines, however not in the higher temperature magnesium line, showing that macrospicules can be found at transition region temperatures, but will not rise to coronal temperatures. The authors find the macrospicule to be 31 Mm in height and 13.3 Mm in width, agreeing with previous values.

The bright roots evident in the O V lines begin to form the 'inverted-Y' shape, typical of the standard jet formation mechanism outlined by Shibata et al. (1992) (more to follow). As a result of this, Pike and Harrison (1997) go on to discuss the nature of the feature and whether it is a macrospicule or X-Ray jet. Pike and Harrison (1997) conclude that this feature is still classified as a macrospicule, due to the observations in He I and the feature adhering to the properties highlighted in Bohlin et al. (1975).

Building on the work done by Pike and Harrison (1997), Parenti et al. (2002) undertook an extremely detailed case study of a macrospicule observed in CDS. In this case the observations are still reliant on the macrospicule protruding above the limb, and observed using the full suite of spectra available to the authors. When discussing these papers, we must consider the rastering method of CDS. The images are comprised of vertical columns of pixels that are exposed for 30 s; the instrument then has a cool down phase before moving onto the next vertical slit. This takes approximately 240 s, which is inappropriate for a feature which on average doesn't have a long lifespan. Because of this delay, the pixels in the x direction, from one column to the next, are separated by a time of 272 s. This means that we cannot consider the spatial structure in the x direction as continuous. As a result of this the authors use the columns of the image array to identify the temporal resolution of the macrospicule.

Parenti et al. (2002) find that the macrospicule extends to 26 Mm and reaches a maximum velocity of 81.6 km s^{-1} and an average outflow velocity of 26 km s^{-1}. The spectroscopic nature of CDS allows for the calculation of temperature and density. As the full range of CDS's GIS suite is being used, the density is not strictly a single number and will be dependent on the emission in the various wavelengths. The density is highest in O IV, 1.5×10^{10} and varies throughout the lines but generally dropping to the order of 10^8 by the Si IX line. The temperatures are calculated as ratios between emission lines, *e.g.* O V 62.97 nm / O IV 55.45 nm, giving values around 2.0×10^5 K, which the authors demonstrate is hotter than the surrounding atmosphere at that point, agreeing with previous works by Habbal and Gonzalez (1991).

As instrumentation improved, the use of spectroscopy resulted in the discovery of the rotational behaviour of a macrospicule as demonstrated in Kamio et al. (2010). In this case, the authors are utilising STEREO-A, the Hinode mission and SUMER. STEREO was used to observe the feature in 30.4 for straight-forward imaging, Hinode for dopplergrams and XRT and SUMER for spectroscopic data.

In the lead up to the particular case Kamio et al. (2010) examines, there were multiple coronal jets occurring at the source of the macrospicule over a 9-hour period. When the macrospicule erupted, again apparent were two footpoints at the base of the feature in the 30.4 nm STEREO images, however, in this study there is also a brightening in XRT at the same time. This is one of the first concrete examples of the relationship between macrospicules and X-Ray jets. The authors highlight that the two foot-points then go on to form two threads propagating upwards, into the corona, subsequently utilising the SUMER instrument to detect their motion in detail.

The properties of this particular example in He II 30.4 nm are quoted as 130 ± 30 km s^{-1} for the radial extension of the feature and line-of-sight velocities of the order -15 and -25 km s^{-1}. With respect to the X-Ray jet behaviour, the velocity is measured at 320 ± 30 km s^{-1} and utilising the LOS velocity in He VIII and Fe XII led Kamio et al. (2010) to conclude that the structure of the macrospicule and X-Ray jet and interlinked. Kamio et al. (2010) also highlight the regression of the material back to the limb causing an enhancement in He II, a phenomenon they propose is caused by either heating in the upper part of the feature or a result of the density increase caused by the downflow of plasma.

Bennett and Erdélyi (2015) present a statistical study (which will be detailed in Chapter 3) of macrospicules using SDO/AIA He II 30.4 nm, the authors utilise the ramp to the solar maxima in 2012 to test how macrospicules respond to the solar cycle. The result that the maximum extensions of macrospicules increase to towards the solar max is the built upon by Kiss et al. (2017) who extend the data set and finds that the lengths increase and decrease on a 1 - 2 year cycle.

The helical motion of macrospicules is reported in multiple papers. Curdt and Tian (2011) present observations of macrospicules in the transition region; they present two examples of 'explosive events'. In one case the feature is on the disk and in the second is above the limb. The discussion at the heart of the paper is differentiating between (RRE/RBE) pairs and helical motion, as observed in Kuridze et al. (2015), due to the fact that they can be misinterpreted in the data. In this case, the rotational velocity evident in the dopplergram images demonstrates symmetrical flow of the order 40 km s^{-1} for both examples. Using the slit modes of EIS, the authors rule out the possibility of lateral movement as a result of bidirectional

RRE/RBEs, calculating that if this were the case, then the jet would be up to 7.2 Mm in each Doppler component. This leads to the conclusion that the jet evident at the limb is moving helically, and consequently, that the feature observed on the disk is also a single jet rotating helically.

This is not the only formation mechanism for macrospicules proposed by the solar physics community; Murawski et al. (2011) describe an upward velocity pulse mechanism. Murawski et al. (2011) used the FLASH code, devised by Lee and Deane (2009), to solve a two dimensional scheme simulating the results of an upward velocity perturbation. Utilising both vertical and oblique magnetic field lines, Murawski et al. (2011) were able to generate a feature with very similar properties to an example macrospicule observed in AIA/SDO. The upward perturbation of plasma increases in amplitude with height, due to the decreasing density of the atmosphere, steepening into a shock. This shock, now in the upper chromosphere, launches cool 'spicule' material below. However, the size, velocity and height are more akin to macrospicules.

Kayshap et al. (2013) present a similar model to Archontis et al. (2005), with small scale flux emergence in the form of a magnetic tube containing an inherent kink, subsequently developing into the Ω shape. The two halves of the tube meet at the bottom, triggering internal reconnection. The resultant macrospicule reaches 12 Mm in height, however, there is also a significant lateral drift. Kayshap et al. (2013) attempt to marry these observations with a two dimensional model, again using FLASH, and manage to produce similar values for the height, but not the observed drift. The amount of energy released by the macrospicule event is dependent on the location of the reconnection site, either high/low chromosphere or transition region. The velocity pulse resulting from this reconnection then goes on to initiate the slow speed shock as seen by Murawski et al. (2011).

2.1.1 EUV Coronal Jets

While spiciules and macrospicules are confined to the chromosphere, we also observe jet like features higher in the hotter atmosphere. One of the most comprehensive sets of jet observations is undertaken by Madjarska (2011), in which the author observes a jet in an equatorial coronal hole, utilising SUMER on SoHO, EIS and XRT on Hinode and the EUVI instruments on the STEREO A and B. The authors find that the jet can be heated by microflares at the moment of reconnection, raising the temperature up to 12 MK. The feature was found during a period of observing brightening in the quiet Sun and coronal holes, where the subject appeared as a jet-like feature emanating from a pre-existing coronal bright point.

The authors demonstrate an unequivocal shaping of the origin akin to that of the Shibata standard model (Section 2.2) The event began with an increase in intensity at the original bright point, extending to a 3 - 4 arcsec^2 area, which the authors identify as a micro-flare. As a result of difference imaging, the authors then concluded that there were several reconnection events during this brightening phase. The expanding plasma in the BP is shown to have a multi-thermal structure, with the first blue-shifted material spotted in hotter emission lines a full minute before the cooler material appears. These reconnection events continue to deposit energy into the jet-like feature, and upon each delivery of energy, an outflow occurs. The slowing down of the outflow also coincides with visible downflows in the underlying BP. During these accelerations, the plasma was shown to have a maximum velocity of 310 km s^{-1}, while no red-shifted down flow was observed at the same time as the energy deposits, which would suggest that this is not a case of a bidirectional jet. The jet is seen to last for 18 minutes, however the first energy deposit occurred 27 minutes before the spire of the jet was visible. The authors note that their observations fit particularly well with the model presented by Moreno-Insertis et al. (2008), in which a current sheet is shown to form at the boundaries of the jet.

Reconnection alone is disputed as a driving mechanism, Cirtain et al. (2007) propose that a series of reconnection events are driven by Alvfén waves. The authors observe initial acceleration of the jet material at 800 km s^{-1}, close to the Alfén speed, coinciding with the relaxation of the magnetic field. These mass outflows appear multiple times during the same jet, as such, the authors conclude that the reconnection is likely being driven by Alfvén waves.

Recent studies have demonstrated the prevalence of smaller scale jets at the magnetic network boundaries. Tian et al. (2014), and later built on by Narang et al. (2016), highlighted these features using the most recent addition to the solar observational tools available to us, IRIS. The network boundaries are regions where there is a great deal of magnetic complexity and strong field values, and almost certainly a large amount of reconnection will be apparent..

Narang et al. (2016) find explosive upflows in the direct images from IRIS with velocities of $80-250$ km s^{-1} and using the superior resolution of IRIS identify jet-like features developing from the bright networks. These jets are long and thin features, 4-15 Mm in length and are approximately 0.3 Mm in width, and demonstrate upflows, with no downflows evident. These events are extremely shortlived, with lifetimes measured at 20-80 seconds, however, there is recurrence observed with jets forming repeatedly in the same location, with time scales in the range 2-15 mins. The jets are also shown to be intermittent but effectively a continuous source of mass, and therefore energy, into the solar wind. As such, Narang et al. (2016)

propose these network jets as new mechanism for generating the solar wind.

2.1.2 X-Ray Jets

Throughout the solar atmosphere, we observe much larger jet-like features than spicules. They have been observed extensively, and not solely in the chromosphere. The first observations of more large scale jets were undertaken using the soft X-Ray telescope on board Yohkoh [Tsuneta et al. (1991)]. Shimojo et al. (1996) undertook the first statistical study of jets, finding a nice round 100 examples to study. With any study looking for specific features, the authors utilised the following selection criteria: 1) that the plasma was collimated and that the movement of the feature was in the direction of the collimation; 2) the aspect ratio of length to width is greater than 3; and 3) the time between the pre-jet image and the image in which the jet first appears is less than an hour. These are an excellent example of selection criteria which aide in forming the search, however, they are broad enough not to introduce bias into the sample.

The authors find that the jets are primarily initiated by a microflare/sub-flare at the base/footpoint (the terms are used interchangeably in literature) of the jet, sometimes apparent as a bright point. They find their lengths to be of the order 10 - 400 Mm and widths are of the order 5-500 Mm. Velocities along the direction of collimation are observed to range between 10 and 1,000 km s^{-1}, averaging at approximately 200 km s^{-1}, and lifetimes can be up to 10 hours. In terms of physical evolution of their shapes, the authors find that 76% of the jets demonstrated converging shapes, *i.e.* the width of the jet would be constant over its evolution or decreasing with distance from the footpoint. The constant form were found to come from a wide variety of apparent source configurations, whereas the converging forms were, explicitly formed from energetic points. This work has formed the basis of much of the study of jet phenomena, however, this is merely an exploratory study around which future studies have been expanded.

2.2 Models and Jet Formation

Numerical simulations play an essential role in developing our understanding the nature of jet formation as observing the chromosphere can be a complex challenge.

What has become known as the standard model for the formation of solar jets is demonstrated by Shibata et al. (1992). Within this paper, the authors use the soft X-Ray telescope on Yohkoh to examine 20 jets, and present their spatial properties, very similar to those of Shimojo et al. (1996), but the authors go on to describe a

possible formation schematic. The model is based upon the flux emergence from the lower solar atmosphere, and is backed up by data in the Solar Geophysical Data. The authors demonstrate that the observations reveal a void at the jet base, similar in appearance to voids observed in reconnection-driven events such as flares and CMEs. They proposed that the jets are rooted in the chromosphere, based on an inspection of the emission measure. Consequently it is likely that the mass is from the chromosphere. The authors go on to posit that the undulating and meandering shape of the jet lends itself to a helically twisting magnetic structure, suggesting that the jet itself emanates from a relaxation of the magentic field along a global flux tube Shibata and Uchida (1986). Such a reconnection event between twisted and untwisted magnetic field would be capable of producing a jet of this size, lifetime, and more importantly, velocity.

This model for the standard jet requires that there be open magnetic field lines, and that a smaller-scale, twisted, emerging flux loop rise from the lower atmosphere in order to initiate a reconnection event. As a result of the reconnection event, material in the emerging loop is then transferred into the open magnetic field lines, 'sling shotting' around the loop it was formerly a part of and up the open field lines, thus creating a collimated beam of plasma. The mechanism highlighted in this particular model produces exclusively narrow jets, a couple of megameters in width. It also results in the dissipation of large amounts of energy which manifests as brightenings in many observations. From the source of the reconnection, energised plasma then dissipates down the loops highlighting the entire structure. The visual effect of the long, collimated beam/plasma spire and the newly brightened loop of plasma, reveals an 'inverted-Y' shape or Eiffel tower-like structure, similar to the 'cusp' shape observed in significantly larger features high in the corona round streamers and flares [Vourlidas (2006)]. These terms have gained common usage in literature and will be used hereafter.

An excellent example of this type of formation is demonstrated in Nishizuka et al. (2011). Within this work, the authors demonstrate what is referred to as an anemone jet, so called as the dome-like bipole magnetic bubble resembles the sea creature. The model they build as a result of this is in three dimensions - consequently, the small scale loops of the standard model could be projected into 3D as an anemone-like shape. The authors observed the jet in Ca II, it formed along an inclined line approximately 45° away from normal, in the inverted-y format. With the jet forming in Ca II, we can conclude that this particular jet is formed in the upper chromosphere, and with this particular jet the authors observe the formation loop itself. The jet feature is found to extend 14 Mm into the atmosphere with a width of 6 Mm, and a maximum velocity of 100 km s^{-1}. However, this maximum is

observed 10 minutes into the evolution of the jet, contrary to what you might expect.

The standard jet model accurately describes a prominent section of the jet population. Those which it does not cover are highlighted in Moore et al. (2010). The specific example that the standard jet model does not cover is the case where the width of the jet is more than that predicted by the standard model. Moore et al. (2010) utilise Hinode/XRT to look for X-Ray jets occurring in the polar coronal holes, and where possible the authors observed the same features in EUVI as well.

The initial magnetic field topology is largely similar to that of the standard jet, consisting of a small-scale loop within an open magnetic field region extending upwards. The difference in these models is that the emerging bipole arch in the case of the standard jet remains untwisted and without shear. In the case of blowout jets, this arch/loop is sufficiently twisted and sheared that it can drive an explosive eruption. In terms of the physical evolution, there is no difference between the two until the emerging flux element triggers a reconnection burst at the boundary between said emerging flux and the open magnetic field lines.

The authors then go on to suggest two resolutions to the reconnection event; the first is that the boundary becomes unstable on its own, and consequently reconnection begins on its own. This results in breakout reconnection, expelling the loop's outer magnetic field, which lifts the restriction on sheared flux lower in the system; consequently allowing the core of the emerging flux to erupt upwards. This forms a chain event, with emerging core events causing more reconnection and consequent releases and so on, similar to Antiochos (1998). The second permutation is that the sheared core begins to erupt before any reconnection takes place at the boundary. In this scenario, an instability in the emerging bipole causes the previously stable core to begin emerging. As a result, magnetic pressure at the boundary current sheet between the loop and open magnetic field, increases to the point at which breakout reconnection is triggered.

This work clearly has an impact on the current relationships between the various jets of scales larger than spicules (which clearly are their own feature). The authors propose that the blowout jets correspond to the macrospicule features in the chromosphere, more on which later. As for implications with respect to the division of standard and blowout jets, observations of the formation mechanism would clarify the feature. Standard jets would have large originating loops spanning approximately 20 Mm or are not visible at temperatures lower than 10^6 K, whereas blowout jets need to produce strong signals in Hα and He 30.4, due to the cooler plasma thrown upwards from the unstable magnetic bipole emerging.

Chapter 3

On the Statistics of Macrospicules

3.1 Introduction

Noticeable in Section 2.1, is the lack of recent statistical studies. A statistical study would be particularly pertinent at this time, given that we now have a generation of advanced instruments with extensive catalogues of data. It is now possible to re-examine the properties of macrospicules (MS) and improve the picture yielded in previous studies *e.g.* Bohlin et al. (1975) and Dere et al. (1989). Furthermore, MS are chromospheric objects which project upwards into the transition region, hence understanding MS could enhance our knowledge of the region from the chromosphere up into the corona. We also need to confirm the features' place amongst the plethora of solar ejecta; jets, surges, rapid blue, or red, extensions, ordinary spicules to name a few Tsiropoula et al. (2012).

The focus of this chapter is an observational discussion of what a macrospicule is; we present a set of characteristic spatial properties for the population of MS investigated as well as the evolution of the structures, and also an inquiry into whether the properties of the MS have any proxies to the solar cycle.

In order to analyse any potential relations over a solar cycle the sample of MS will be taken over a time span of many years. Hence, we will use the 30.4 nm bandpass from the Atmospheric Imaging Assembly (AIA) camera on-board the Solar Dynamics Observatory (SDO) Lemen et al. (2012) which has been in place and operating since June 2010. As this was the epoch of the last solar minimum, we will take the sample through from this date until the end of 2012. This range will capture the ramp from solar minimum to the period which is estimated to be close to the solar maximum. In order to gain a significant sample size we will take two samples of two hours for each month during this period.

In Section 3.2 we present the relevant techniques used to take the measurements

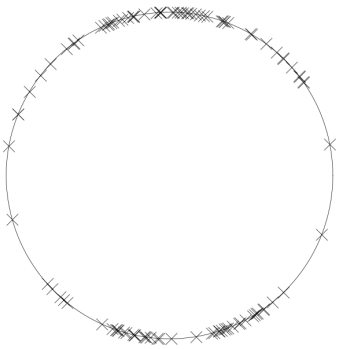

Fig. 3.1 The location of the samples of MS displayed at the limb, indicated by the crosses.

and the instrument utilised. Section 3.3 presents the results of the study and discusses the consequences, specifically, with respect to the general spatial properties, followed by finding patterns over the sample time period and, then, a study of their evolution. Section 3.4 contains our conclusions. The work was published in Bennett and Erdélyi (2015).

3.2 Observations

The AIA instrument on-board SDO delivers 4096 × 4096 pixel images with 0.6 arcsec/pixel spatial resolution and a 12 s cadence Lemen et al. (2012). Raw images were processed using SunPy [SunPy Community et al. (2015)], into a flattened-out limb such that the horizontal axis is the azimuthal angle and vertical is radius from the centre of the field of view. This allows a better measurement of the spatial properties of MS.

The MS were selected based on satisfying the following criteria:

- The evolution of the macrospicule is visible, *i.e.* the extension from the chromospheric surface to its maximum height and consequent regression back to the limb. This excludes examples which appear to disintegrate at some point during its evolution or the retraction of which is not visible.

- The footpoint of the macrospicule was exactly on the limb, rather than inside of or behind the limb. Avoiding the MS which were too far inside the limb was aided by a limb indicating line, drawn based on information from the fits header files. Those events visibly crossing that line were not measured. It was harder to determine whether the MS were behind the limb, but we made our best effort to ensure that the measured MS were in the plane of sky, based on our inspection of the 30.4 nm movies.

- The objects were no longer than 200 arcsec; there are values for maximum length quoted in Bohlin et al. (1975) and Dere et al. (1989), however, we would like to test the length limits of MS in order to more accurately define these phenomena. There is also a lower limit imposed upon us by the data itself. The so called 'forest of spicules' at the solar limb prevents us from measuring any features with a maximum length of less then 5 Mm. We also call into question whether the features observed by those earlier authors were actually MS, there is certainly significant overlap in the lower percentiles of the population of spicules and MS.

Each 30.4 nm image was analysed separately and the length of the macrospicule in question is measured, defined here as the distance between the foot and tip of the macrospicule. We then took the mid point of the line between the foot and tip, and consequently used the mid point as a reference point for measuring the width. We used the bottom of the macrospicule brightening as l_0 and in situations where there was none, we used the lowest point at which plasma motion was initially observed. Using this method, we obtained information on the macrospicule with 12 s cadence. Within the stated sample period we took 2-hour samples on the 1st and 15th of each and every month.

Having undertaken the study, the distribution of the loci of macrospicule events measured along the solar limb is displayed in Figure 3.1. There are 101 examples in this study. Note that there is some ambiguity in measuring spatial properties of features near the limb due to line-of-sight integration. However, without using data observing the MS from multiple directions, the best approximation is that MS are generated in the plane-of-sky, despite the potential uncertainties inherent in measuring at the limb.

3.3 Results and Discussions

Following the analysis of the MS as described above, the properties and, therefore, statistics for the sample of MS are found. Of the sample we find that 30.5% of MS occurred in polar coronal holes, 20.0% occurred at the coronal hole boundaries and 49.5% were found in the quiet Sun. The coronal hole boundary is defined loosely as the region where the coronal hole and quiet Sun meet. It is evident in the 30.4 nm images that the coronal hole is significantly dimmer than the quiet Sun. Where these two regions meet, the quiet Sun and coronal hole structures combine over roughly 10 Mm. If a macrospicule is neither clearly in the quiet Sun or coronal hole in this region and within this region, it is defined as being in the coronal hole bound-

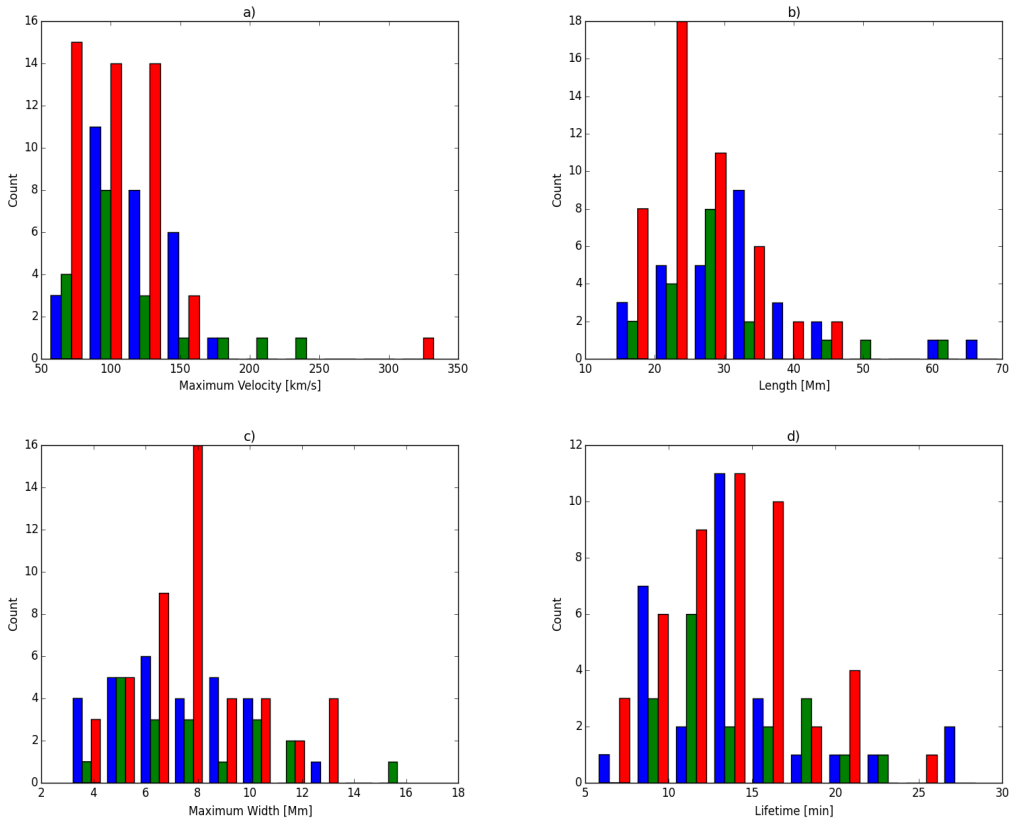

Fig. 3.2 Figure taken from Bennett and Erdélyi (2015). Histograms of properties of MS. In each bin counts from the 3 solar regions are displayed separately Blue indicates coronal hole MS, green represents coronal hole boundary MS and red are occurrences in the quiet Sun. a) top left. Histogram detailing the values of maximum velocity over the sample period. General grouping around the mean for all regions, 109.7 km/s, and an absence of clear distributions is evident, particularly in the quiet Sun, top left. b) top right. Detailing the maximum lengths, separate behaviour is found for all regions, quiet Sun displaying a distinctly lower peak, top right. c) bottom left. Maximum width of the MS, irregular distributions are clear with very little difference between the regions, bottom left. d) The lifetimes again show little difference in range, however MS at the coronal hole boundary have a slightly higher mean, bottom right.

ary. Macrospicules generated near complex magnetic regions were not measured, due to the possibility of these regions influencing the measurement or of falsely identifying a feature as a macrospicule. Since active regions qualify as regions of complex magnetic field, MS forming in their proximity were excluded.

3.3.1 General Properties

We begin with constructing the histograms for the individual properties, *i.e.*, distribution of velocities, lengths, widths and lifetimes. Examining these general proper-

ties, we will consider each property in terms of the magnetic environments.

Beginning with the maximum velocities in Figure 3.2a, note the almost uniform distribution of MS found in the quiet Sun between 50-150 km/s falling steeply after. The outlier in the 300-350 km/s band is a value which may have errors. The respective range and mean values are, for the quiet Sun: 54.1-335.1 km/s and 105.2 km/s, for coronal holes: 58.3-181.0 km/s and 113.4 km/s, and for coronal hole boundaries: 66.8-236.0 km/s and 114.5 km/s. These values are quoted with an error on each value of ±2.2 km/s.

We observe similar maximum velocity mean values for coronal holes and coronal hole boundaries while the quiet Sun has a lower average maximum velocity. This could imply different generation processes for MS in the coronal holes and at coronal hole boundaries, where reconnection is evident Patsourakos et al. (1999) and is a possible source for MS (see Heggland et al. (2009)). However, there is not enough evidence to conclude that MS are produced differently in other magnetic environments. Within the coronal hole it has been proposed that a collection of smaller spicules forms a macrospicule Scullion et al. (2009), which would explain similar mean maximum velocities.

Where the maximum velocity occurs over the trajectory of the macrospicule is important, particularly for future modelling. We find that the maximum velocity of the macrospicule occurred within the first 19% of the macrospicule's evolution in 68% of cases.

Figure 3.2b shows the maximum lengths of all macrospicule instances. Investigation reveals ranges and means as follows, with errors of ±1.5 Mm; coronal hole lengths range of 17.3-69.8 Mm with a mean 31.9 Mm, at coronal hole boundary the range is 16.1-60.2 Mm with a mean 30.2 Mm and for the quiet Sun the range is 14-45.3 Mm with a mean of 25.4 Mm.

We observe similar means and ranges for the lengths of the coronal hole and coronal hole boundary populations. This is unsurprising due to the open field nature of both regions allowing extension up the field lines. Whereas, in the quiet Sun, the mean value is 18% less than those observed in the coronal hole/boundary. We draw attention to the narrower range in the quiet Sun as well. These values could be the consequence of the more complex magnetic field above the feature not allowing as much growth.

From examining Figure 3.2c, detailing the maximum width of each macrospicule, it is evident that there are no distinct peaks in any of the populations in the coronal hole/boundary regions. After investigating the means, very similar values are revealed, 7.2, 7.9 and 7.8 Mm for coronal holes, coronal hole boundaries and quiet Sun, respectively. The mean value for the quiet Sun coincides with the peak, but

again, has no mathematically definable distribution. Of interest is the ratio between the width and length of MS, particularly useful in reference to modelling. Values found are; for coronal holes, 0.24, for coronal hole boundaries, 0.26 and for quiet Sun 0.32, demonstrating that the width is small compared to the length of the macrospicule. Finally, it is evident that MS in the coronal hole/boundary regions have a lower ratio value than instances in the quiet Sun regions.

The lifetimes (Figure 3.2d) have a similar lack of difference between the populations seen in the width distribution. Ranges and means are as follows; for coronal hole 7.8-28.6 min and mean 13.4 min, for coronal hole boundary 9.8-22.0 min and mean 14.4 min, and for quiet Sun 5.6-30.6 min and mean 13.6 min. The values obtained show similar ranges for coronal hole and quiet Sun instances but a smaller range for MS at the boundary. However we suspect that these are insignificant as the error in lifetime is ±1.1 min, implying that the means are similar for all three magnetic environments.

These values, found during the present analysis, are in-between the sets of values put forward by Bohlin et al. (1975) and Dere et al. (1989).

3.3.2 Inclination

From previous studies it has been noted that MS have inherent inclination. Bohlin et al. (1975) noted that the further from the pole of the Sun the greater the inclination of the macrospicule. It is worth noting here that they did not in fact consider any MS outside of the coronal holes.

We plotted the MS according to latitude and magnetic environment, Figure 3.3. This graph shows the latitudes of each macrospicule instance against the degree of inclination; there are clear indicators where the coronal holes are. What is noticeable at this point is the fact that lower inclinations are associated with the ordinary coronal hole features but that MS occurring at the coronal hole boundary have a greater inclination, with no events which have a value lower than 15°. Quiet Sun events have an almost uniform distribution even appearing to occur in a coronal hole, but this is an artefact of the size of the coronal hole changing with the solar cycle and becoming very small as the Sun nears the solar maximum.

3.3.3 Relation between macrospicule properties

It is worth investigating whether the properties, discussed earlier, have any empirical relation to each other. Figure 3.4 shows the relationships between the maximum length, maximum velocity and lifetime of each macrospicule observation. Inspect-

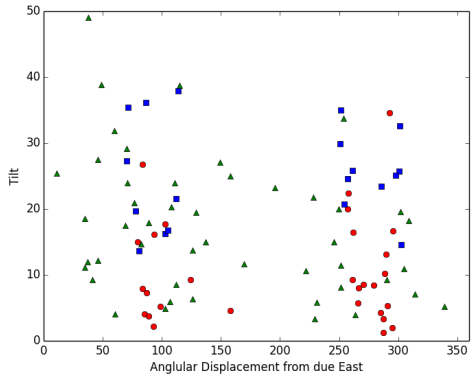

Fig. 3.3 Figure taken from Bennett and Erdélyi (2015). Macrospicule events are plotted in terms of latitude and inclination. Inclination is defined here as the angle away from the normal to the limb of the Sun. The latitude is defined from due east and traces out anticlockwise. The red circles here are instances in the coronal hole, blue squares are at coronal hole boundaries and the green triangles are quiet Sun.

ing Figure 3.4a, reveals a clear correlation between the maximum length and the maximum velocity, as indicated by the least-squared regression,

$$v = 61.3(1 + 0.28L), \tag{3.1}$$

where v [Mm/s] is velocity and L [Mm] is the maximum length, the normal residual of which is 0.43, indicating a significant fit. There is a particular exception in the top left of the plot which may have some errors and has altered the slope of the regression line quite distinctly.

There is a similar pattern to be reported in Figure 3.4b, where the lifetime and maximum length have been plotted against each other.

$$L = 10.39(1 + 0.12T), \tag{3.2}$$

where L length in Mm and T is the lifetime in min and normal residual value 0.66. This value is small compared the average maximum length, therefore the fit is reliable. Again, there are a few extreme instances which may not be a part of the overall macrospicule population, such as the instance in the bottom right with a short maximum length but long lifetime.

Lastly, Figure 3.4c, shows the relationship between the maximum velocity and the lifetime of MS, defined,

$$v = 88.9(1 + 0.016T). \tag{3.3}$$

Incongruously, relationship between the maximum velocity and the lifetime of

the MS is unclear. A shallow trend is apparent in the scaling factor, 0.016, which is inconclusive as to whether a relationship exists between the two properties, however it is unlikely.

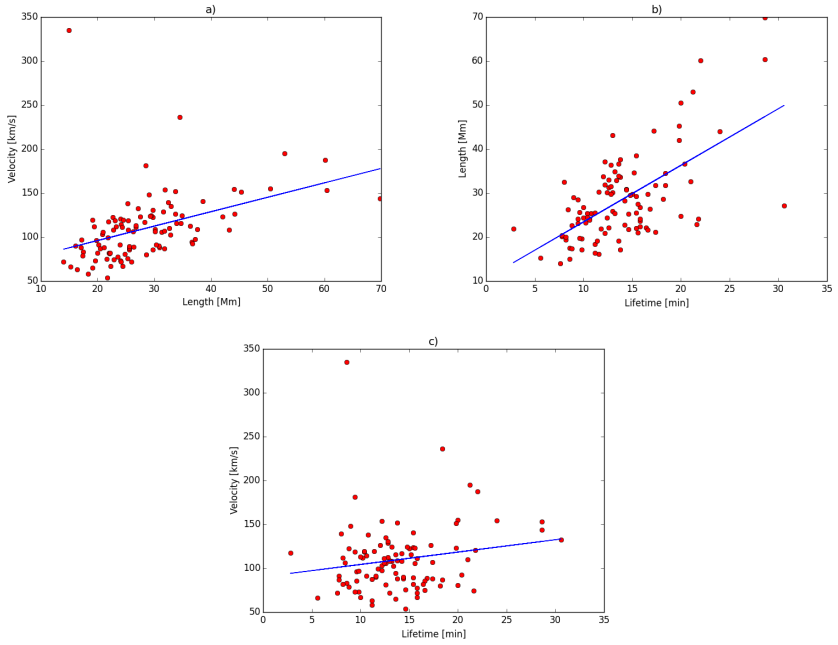

Fig. 3.4 Taken from Bennett and Erdélyi (2015) Properties of MS features plotted with respect to each other. a) Top: The max length against the max velocity for each individual instance. The least-squares fit shows a distinct correlation. b) Middle: The lifetime vs max length graph shows a similar degree of correlation between these two properties, middle. c) Bottom: In the case of max velocity and lifetime, there is no such relation, as is indicated by the least squares fit and scaling equation (below). Error bars associated with the least squares fit are omitted as the standard error is small compared to the range of values.

3.3.4 How the macrospicule general properties change over the sample period

The investigated sample period is a proxy for the process by which the Sun's activity increases from solar minimum in 2010 up to solar maximum at the end of 2012. Therefore, examining the macrospicule properties over the sample period is a worthy exercise and may give insight into the cause of MS. Figure 3.5 illustrates how the general properties alter over the sample time period. Examining first the maximum length, Figure 3.5a, shows a relationship over the entire sample period, with some instances where the maximum length values do not appear to be part of the overall population.

However, these examples, which are over 50 Mm, are not necessarily too extreme

to be classed as MS. Upon visual examination of the five most extreme examples there are no discernible differences in the four instances between 50 Mm and 60 Mm in height. The most extreme example, 69.8 Mm, does appear separate from the population. It is wider than average and the structure is less defined and more fractious. This can be removed from the sample. The mathematical relation of the fitted line, using least squares, reflects the general trend upwards over the sample time period,

$$L = 24.9(1 + 0.11t), \tag{3.4}$$

where L is the maximum length of a macrospicule and t is the point in time. The gradient value is small, but is a result of the long period over which the sample has been taken.

Studying the lifetime property of the MS over the solar cycle in Figure 3.5b we, again, notice an increase over the sample-time period, though the gradient is not as steep as that of the fit for the maximum lengths,

$$T = 12.7(1 + 0.074t), \tag{3.5}$$

where T [min] is the lifetime of a macrospicule and t is the time [years]. There seems to be a general population close to the fit with only a few extreme examples, e.g. one below the general population and 3 above 25 min. We closely examined the extreme examples in this case as well. Only the macrospicule with the longest lifetime showed any particular differentiation from the rest of the population. Greater width is observed alongside apparent separate structures within the macrospicule, therefore this instance is eliminated from the study.

The most interesting result here is that when inspecting the maximum velocity over the sample period, see Figure 3.5c. We notice that the maximum velocity changes very little, the magnitude of the gradient is indicative of a small decline,

$$V = 113.03(1 - 0.025t), \tag{3.6}$$

where V is the maximum velocity in Mm/s. Given that we found that in Figure 3.5c, the maximum length and maximum velocity are related, one would naturally expect the maximum velocity to show a similar behaviour over the sample time period. Again, we visually examined the extreme examples eliminated two instances, a maximum velocity of 335.9 km/s was clearly an error in measurement and so has been removed and the second is not clearly defined and may have suffered from limb effects. (All extreme examples are included in the graphs here, but however are

excluded from our final statements.)

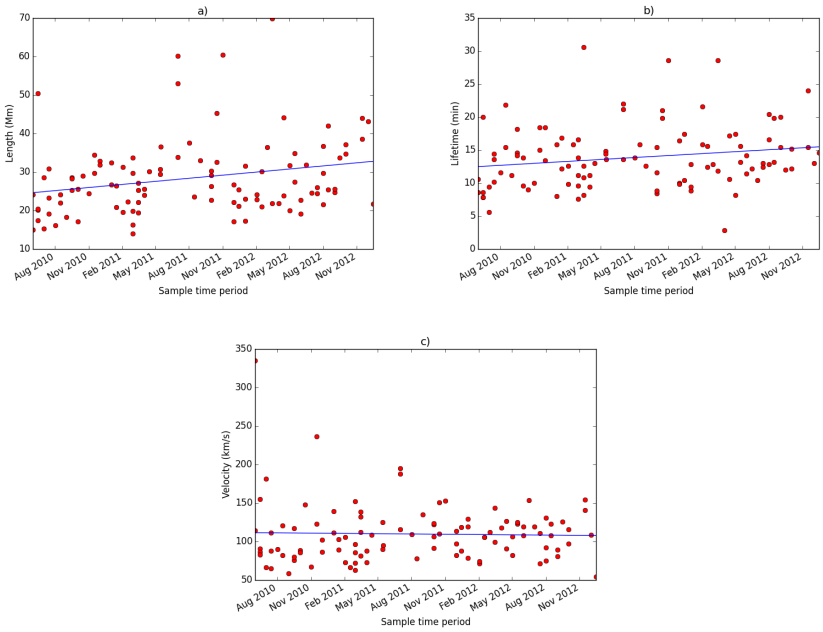

Fig. 3.5 Figure from Bennett and Erdélyi (2015). Macrospicule properties over the sample time period. Notice that the graphs for maximum length and lifetimes, a) top and b) middle, respectively, have general trends with a positive gradient over the sample time period, while the maximum velocity graph, (c, bottom panel) has none of the same trends apparent in the others.

3.3.5 Ballistics

How the features behave over their life-span is important in terms of possible generation mechanisms, and how they may interact with the transition region. SDO has limited spectral data as AIA is an imager. Therefore, readings are limited to spatial measurements. One interesting question is whether MS have a ballistic nature such that upon reaching their highest point they would then fall back only under the influence of the Sun's gravity. The question is of importance due to the nature of ordinary spicules typically located at granular lanes.

Current research proposes two varieties of spicules, type-1 and type-2, Pereira et al. (2012), but Zhang et al. (2012) debates this point, and finds no such population split. We believe that names of physical phenomena should be based on the underlying physics, not arbitrary behaviour. Type-1 spicules are potentially driven by p-mode global oscillations, and spicules typically have lifetimes of 4 - 10 mins and heights 7 - 10 mins De Pontieu et al. (2004).

Type-2 spicules are most likely reconnection events, which might explain their

high velocities, similar lengths to type-1 and typically observed with much shorter lifetimes, 10 - 150 s, Isobe et al. (2008). Type-2 spicules are observed not to fall back to the solar surface, however, there is debate as to whether these features are physical, or an artefact of observation Tsiropoula et al. (2012), Sekse et al. (2013) or finally whether their regression is observed in a different wavelength Pereira et al. (2014).

The question becomes: are these MS giant versions of *p*-mode spicules, or are they blown-up manifestations of reconnection spicules. Alternatively, are they related to these ejecta at all? In order to answer these questions, one needs to understand what the underlying driving mechanism for Type-1 and Type-2 spicule. Consequently, one needs to find signatures of driver(s) in the formation of MS. An interesting alternative suggestion for generation of MS is a model where multiple spicules form a macrospicule Xia et al. (2005).

The final case is that MS and spicules are not related in their formation at all. Shibata et al. (1992) proposed a jet formation model which has become known as the 'Inverted Y' jet model which occurs on much larger scales than spicules. Using Yohkoh's soft X-Ray Telescope (SXT), they highlighted the X-Ray jets had lengths in the 5-40 Mm and velocities in the order 30-300 km/s, notably, similar to the values we have quoted above. This fits in with the observations of Moore et al. (1977) of X-Ray bright points coinciding with Hα MS, (also supposed in Kamio et al. (2010)). Another model presented by Jiang et al. (2007) proposes magnetic flux emergence as a source for Hα and EUV jets. They find lengths similar to those discovered as well, 4-22 Mm with a lifetime range of 10-34 mins (including cool and hot aspects of the jet). Both values are also comparable to those we observe in this study.

Given this, one might expect that there is a consensus that these are the same objects observed in different wavelengths, however, this is not the case. Moore et al. (2010) highlight a dichotomy in solar coronal jets, certainly between the standard jets Shibata et al. (1992) and blowout model for jet formation which the authors described. The authors concluded that the blowout jet model results in Helium 30.4 nm MS forming from base arches of the order 10 Mm in width. If we assume that MS observed in Hα and Helium 30.4 nm are the same feature as supposed by Labonte (1979) and implied by Parenti et al. (2002), then is it reasonable to propose that the blowout jet mechanism also drives EUV MS.

Examining Figure 3.6 there are two particular trends to note. The first is shown in Figure 3.6a, where the times for the regression back down to the solar limb were taken from the observational values, blue point in the figure, and times calculated using basic gravitational laws, assuming point mass and free-fall under uniform gravitational acceleration from the tip of the macrospicule, are in red.

We observe similar times for regression back to the limb for the estimates and the recorded times. Clearly there is a greater variance in the measured values compared to the estimates, but this is to be expected. The mean time for the tip to recede back to the limb is 7.5 min estimated and 6.6 min recorded, with the similar values indicating that gravity is the dominating force behind their fall. The difference between the two sides of the evolution is 6.6% of the average overall lifetime, which is likely not large enough to be significant.

Let us now make a brief comparison of this behaviour described by the current literature. Recent studies have found that the time taken for a jet to fall back to the solar surface is greater than expected from a ballistic model. Nishizuka et al. (2011) have found that chromospheric jets (small jets, 1-4 Mm in length with a magnetic anemone base) share similar motions with the shock-acceleration model demonstrated in Shibata and Suematsu (1982), notably, slower than a ballistic model. Moschou et al. (2013) also find velocities lower than those under a ballistic model, however, the features highlighted here are much larger, measuring 100-190 Mm in length, than MS. Feng et al. (2012) demonstrate that kinematic motions of the particles in jets follow ballistic trajectories. Therefore it is possible that in MS the plasma-beta is high, and the entire feature follows the ballistic nature of the gas particles. Otherwise, the observed motion may be due to the surrounding magnetic environment. Macrospicules examined here were deliberately chosen in locations where there was a lack of complicated magnetic environment, hence would be allowed to evolve on their own.

Figure 3.6b, demonstrates the change in width either side of the greatest extent of the macrospicule as a percentage. We find that after the peak of the macrospicule, the width actually decreases on average with MS being 20% smaller. This could be due to plasma flowing down magnetic field lines causing a thinning within the macrospicule. This could delay the collapse of the macrospicule and cause the slightly longer recorded times as opposed to the estimated times.

3.3.6 Energetics and scale-height

Examining the energy required to generate MS is a worthwhile task, in reference to the process to which they are formed. At the limb $g = 276$ ms^2, hence, the gravitational scale-height will need to be taken into account when performing any calculations. Pereira et al. (2012) has studied this behaviour in the case of spicules, however, no such study has been performed for MS to date. We have modelled the MS simply as a column of plasma, with no magnetic field influences, and considered the potential energy required to reach the height at which they are observed.

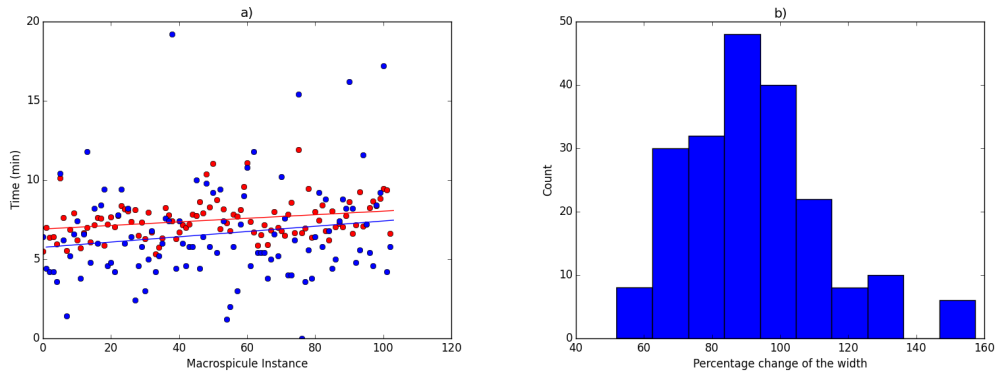

Fig. 3.6 Estimated times for a point mass falling from the apex of the macrospicule trajectories, a) top, for the macrospicule are red, while the times taken from the data are blue points, top panel. There is little deviation from ballistic model evident in the MS measured times. b), bottom, the percentage change in width. The widths are taken before and after the peak of the length-time plot as a percentage change. The width is smaller, on average, after the peak.

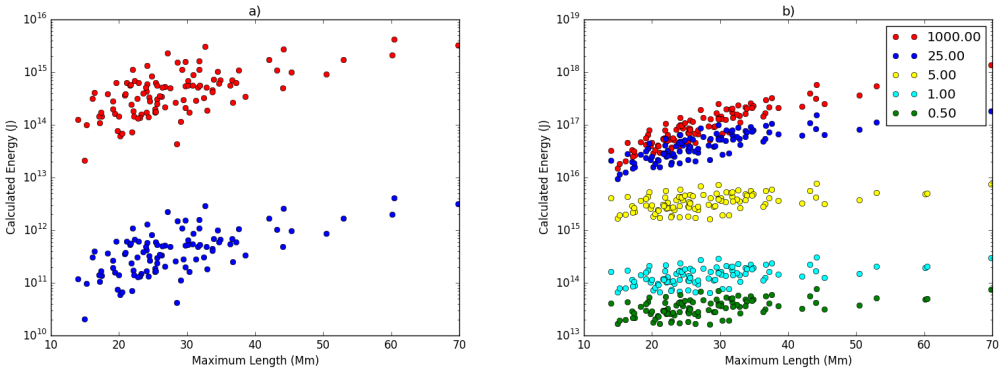

Fig. 3.7 a) Here we have used two different ρ_0 values. Red indicates $\rho_0 = 1.0 \times 10^{-8}$ kg/m^3 and blue indicates $\rho_0 = 1.0 \times 10^{-11}$ kg/m^3. b) The energy required to form a macrospicule plotted as a function of the maximum length of the macrospicule. The maximum length is plotted against the energy required to move a mass to this height. The scale-height value of 1000 Mm here is used as a proxy for uniform density as this is approximately 10 times greater than the largest macrospicule in the sample, which, makes the assumption valid.

Choosing a ρ_0 is important, measurements by Parenti et al. (2002) and Withbroe et al. (1976) give densities of MS as 1.0×10^{-11} kg/m^3. However, we assume here a scale-height over the extension of the macrospicule and these authors measure the 'body' of the macrospicule. As such, we use a ρ_0 taken from Vernazza et al. (1981), $\rho_0 = 1.0 \times 10^{-8}$ kg/m^3. Given that we use a scale-height and applying our ρ_0 at the footpoint, we will obtain a sensible value for the energy required to form a macrospicule.

The centre of mass was estimated, and the potential energy necessary to move

the mass from the limb this point defined as:

$$R_y = \frac{Le^{-L/H} - He^{-L/H} + H}{1 + e^{-L/H}}, \tag{3.7}$$

where R_y is the distance from the solar limb, H is the scale-height and L is the maximum length of the macrospicule.

Integrating over the volume of the macrospicule, taking into account the scale-height, estimated the mass. Applying the mass as a point at R_y, the minimum mechanical energy required to form a macrospicule is equal to the potential energy at R_y. Figure 3.7 demonstrates how the estimated energy required will change dependent on the scale-height of the plasma contained within the macrospicule.

As is intuitive, the more uniform the density, the higher the energy required to form the macrospicule. Noticeable are the gradients at higher scale-heights, 1.61×10^{16} J/Mm with uniform scale-height, and, when $H = 0.5$ Mm the gradient is 6.88×10^{11} J/Mm. This is important as the more energy required to form a macrospicule of a given length, the less likely they are to form. Instances of MS in uniform density and with a scale-height of 25 Mm are similar below heights of 25 Mm.

Macrospicules have been proposed as a source of coronal heating. In order to estimate how much mechanical energy could potentially be transferred from the MS into the corona, we will assume that at any given moment, a macrospicule is occurring at the limb. Assuming that measurements taken here are within ±10 Mm of the plane of sky, we take the next interval in which a macrospicule occurs as the angular distance, covering the ±10 Mm over the plane of sky, starting at the boundary of the previous interval.

Extrapolating this around the rest of the solar surface and applying the mean macrospicule count per two hour sample, 1.9, to each interval a power output can be estimated. Assuming further that all mechanical energy is transferred from the macrospicule into the corona, the power output for uniform scale-height MS is calculated to be 0.153×10^{-3} W/m2 and decreasing with the scale-height. Given the power requirements for coronal heating in Aschwanden et al. (2007), MS are an unlikely source for major coronal heating.

3.4 Conclusion

Now, let us summarise the general properties for the population of MS (see Table 3.2). In general, the values presented here fall between those presented in Bohlin et al. (1975) and Dere et al. (1989). The more extreme examples, seen in Bohlin et al. (1975), are not found here. We find that the data in Dere et al. (1989) are conservative

and we find maximum length and lifetimes which are larger.

Examining the individual regions, in which the MS occur, it is evident that higher velocities are found in the coronal hole and coronal hole boundaries and so we consider the question of whether there might be a difference in the physics of formation to that in the quiet Sun. Examining the lengths, the coronal hole/boundary MS are longer than those seen in the quiet Sun. Open magnetic field lines in coronal holes are the likely cause allowing the MS to extend higher in these regions. We find little difference in the widths, and, examining mean lifetime values, we find percentage differences from the total sample mean: 3.7% and 2.6% for quiet Sun and coronal hole boundary respectively, with a small increase in percentage difference of −5.3% for coronal hole MS.

Upon examining the general properties and their relations to each other, we also find that the maximum velocity and maximum length are related, and, that the lifetime and maximum length show signs of correlation. However, the maximum velocity and lifetime appear to show little correlation with the current sample size.

A range of magnetic environments have been shown to yield MS with different basic properties in some cases. This may be due to separate generation processes, although this is just a conjecture. The overlying solar environment is more likely to have an effect, either restricting or allowing extension, which would explain the comparatively longer MS observed in coronal holes.

Considering the change of the properties over the sample time period, we find that the maximum length and lifetimes both show a general correlation with the sample time period. Whereas, the maximum velocity does not follow the same pattern, which is somewhat unexpected due to the maximum length being related to the maximum velocity. Consequently, one might expect the maximum velocity to increase as a function of the sample time period. At present we cannot offer any explanation as to why this is the case, but further modelling studies will hopefully reveal some answers.

We observe similar durations for regression back to the limb for the estimates and the recorded times. Clearly, there is a greater variance in the measured values compared to the estimates, but this is to be expected. The mean time for the tip to recede back to the limb is 7.5 min (estimated) and 6.6 min (recorded), which are similar, indicating that gravity is the dominating force behind their fall. This small difference between reading and model is not large enough to be significant, or draw any conclusions.

Lastly, let us estimate the energy required to generate the MS. We incorporated the scale-height variations over the length of the macrospicule, such that, the density decreases from footpoint to tip. This was applied to take into account non-

uniform density when estimating the centre of mass. We find that high scale-heights yield high energy requirements, which decrease with lower value scale-heights. Examining the mean macrospicule energy values for the scale-heights we obtain 1.46×10^{17} J, 4.78×10^{16} J, 3.09×10^{15} J, 1.46×10^{14} J and 3.66×10^{13} J for scale-heights of uniform and 25, 5, 1 and 0.5 Mm, respectively.

Our simple energetics model yields values for energy which are possibly too small, bit are still realistic. If we compare these to energies calculated for wave-driven reconnection events in Heggland et al. (2009), of the order 10^{17}-10^{18} J , if the scale-height is around 10-25 Mm according to our estimates, the generation of MS may be feasible. However, this model generates jets of 1 Mm in length, a degree of magnitude away from our measurements. Models have been proposed, such as Adams et al. (2014), in which open magnetic field above a reconnection event allows the MS to extend to the heights we observe.

It would be preferable to have 8-10 years worth of high-quality data to examine the possible changes in the properties of MS over the solar cycle. Also, investigating the rotational speed of MS, which is not possible without spectral information, would be feasible and would give additional insight. The use of modelling to understand these features further would also be of interest such that we might be able to understand how these features are generated.

Study	Bohlin et al. (1975)	Dere et al. (1989)	The present study
Max Length [Mm]	5.8-43.5	1.45-16.7 $\bar{x}$:8.7	14.0-60.4 $\bar{x}$:28.1
Width [Mm]	3.6-10.9	2.2-6.5 $\bar{x}$:4.4	3.1-16.1 $\bar{x}$:7.6
Lifetime [min]	8-45	>3	2.7-28.1 $\bar{x}$:13.6
Max Velocity [km/s]	10-150	20-50	54.1-105.6 $\bar{x}$:109.7
Count	25	10	101
Cadence [s]	>180	20,60	12

Table 3.1 General properties table. Comparing the values given by Bohlin et al. (1975), Dere et al. (1989) and this study.

Magnetic Configuration	Velocity (km/s)			Length (Mm)			Width (Mm)			Lifetime (min)		
	Low	High	Mean	Low	High	Mean	Low	High	Mean	Low	High	Mean
Coronal Hole	58.3	181.3	113.4	17.3	60.4	31.9	3.1	13.0	7.2	7.8	28.6	13.5
Coronal Hole Boundary	66.8	194.8	107.4	16.1	60.4	30.5	4.0	16.1	7.9	9.8	22.0	14.0
Quiet Sun	62.8	154.3	101.2	14.0	45.3	25.6	3.4	12.6	7.8	5.6	24.0	13.5

Table 3.2 Properties associated with each region of the solar limb.

Chapter 4

On relationships with an active longitude

4.1 Introduction

Studies of non-uniform distribution of solar activity began with Chidambara Aiyar (1932). Investigations of sunspot groups distribution finds that they tend to cluster towards a certain heliographic longitude [Balthasar and Schüssler (1984); Bumba and Howard (1965); Wilkinson (1991)]. These authors present the concept of an active longitude, at which sunspot groups cluster. As the field advanced, studies have presented the same concept applied to a range of solar features, Zhang et al. (2007) demonstrated this behaviour with solar flares. Benevolenskaya et al. (1999) demonstrate a clustering in surface magnetic fields, and, Mursula and Hiltula (2004) present active longitudes in the heliospheric magnetic field. Lastly, and most applicably to this work, Li (2011) have observed this to be case in coronal streamers.

Macrospicules (MS) are chromospheric objects observed in Hα and He 30.4 nm [Bohlin et al. (1975); Murawski et al. (2011); Scullion et al. (2010); Wang (1998)]. They are explosive jet-like features extending up to, on average, 29 Mm and velocities up to approximately 110 km/s Zaqarashvili and Erdélyi (2009). Their structure reflects the solar atmosphere they move through, they are proposed to have a cool core, surrounded by a hot sheath Parenti et al. (2002). They are of particular use in this study, as they are observed from the solar equator to the poles.

This work presented, was published in Gyenge et al. (2015). This chapter will discuss the longitudinal and latitudinal distributions of MS. Extending this, we will compare the behaviour of MS to those already observed in the studies highlighted above, particularly solar active regions.

4.2 Observations and Databases

The MS were observed using the 30.4 nm SDO/AIA [Lemen et al. (2012)]. This takes a 4096 × 4096 pixel, full disc, image of the Sun at a cadence of 12 s. We took typical samples of two hours, twice a month, from June 2010 until December 2012. For each image the solar limb was flattened out, making it easier to identify and measure the MS. They are extremely difficult to measure on disk, and as such, this study concentrates on those occurring at the limb. We record the time at the moment they become visible at the limb and their angular displacement from solar due east. Measuring MS this way we identified 101 examples of MS. The physical dimensions and the heliographic coordinates have been estimated.

Debrecen Photoheliographic Data (DPD) sunspot catalogue [Győri et al. (2011)] has been used as the source of sunspot groups used to calculate the most prevalent active longitudes. This database builds on from the Greenwich Photoheliographic Results (GPR), which has been the basis of many works in the field. DPD has been used to provide a sample beginning in 1974, detailing every sunspot's area and position since that epoch.

4.3 Statistical Study of the Latitudinal Distribution of MS

In order to examine the spatial behaviour of MS we must measure the Carrington latitudes, B. In order to aid analysis, the Carrington latitudes, B, have been transformed into the following system:

$$\begin{aligned} \phi &= -(B+90^\circ)/90^\circ, B<0 \\ \phi &= -(B-90^\circ)/90^\circ, B>0 \end{aligned} \tag{4.1}$$

The domain of interest of the quantity ϕ is $[-1;1]$. The $\phi = 0$ point contains the northern and southern poles. The $[0;1]$ sub-domain of ϕ represents the northern hemisphere, the ascending ϕ values from 0 to 1 show the descending latitudes from 90° to 0°. The southern hemispheres have been considered in the same way.

Figure 4.1 shows the result of the statistics above. The histogram depicts a normal distribution. $\overline{\phi} = 0.043$, this implies that most of the MS tend to cluster to the poles, as has previously been shown to be the case in Chapter 3, confirming the method. We also find that the northern hemisphere was slightly more active in this time period. The standard deviation values are $1\sigma = 0.3507$ and $2\sigma = 0.7014$.

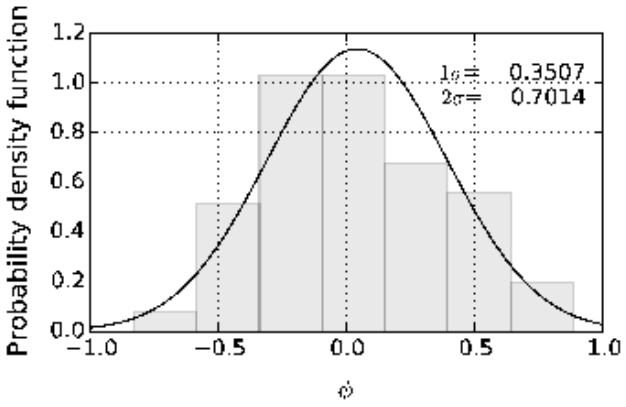

Fig. 4.1 The grey area shows the probability density function of the parameter ϕ. The solid black line is the fitted Gaussian distribution. The values standard deviation 1σ and 2σ of the normal distribution have been indicated in the top right corner.

Hence, 68% of MS measured in this data set, cluster in a 31.5° wide belt from the poles. The extension of this is that 68% of MS are between the ±58.5° and ±90° heliographic latitude, and, 95% of MS are in a 36° degree belt from the poles or between ±27° and ±90° in heliographic latitude. Demonstrating that MS exhibit longitudinal inhomogeneity at higher latitudes.

4.4 Statistical study of longitudinal distribution of MS

4.4.1 Activity maps of active longitudes based on sunspots

According to Gyenge et al. (2014), the method highlighted above has been proven and the active longitude was found to be distinct in each hemisphere. The present investigation started with a similar method as described in Gyenge et al. (2012). In order to construct a complete picture of the active longitudes when considering sunspots, the areas and positions of all sunspot groups are included in this analysis. The solar surface is divided into longitudinal bins of 20° and the areas of all groups were summed up in each bin: A_i in certain Carrington Rotation between 2097 and 2128, the temporal sample over which the MS locations was recorded. Next, the longitudinal activity concentration is represented by the quantity W defined by:

$$W_{i,CR} = \frac{A_{i,CR}}{\sum_{j=1}^{N} A_{j,CR}}, \tag{4.2}$$

where N is the number of bins, $\sum_{j=1}^{N} A_{j,CR}$ is the sum of all sunspot groups in a given CR and $A_{i,CR}$ is the total area of sunspot groups in a Carrington Rotation and

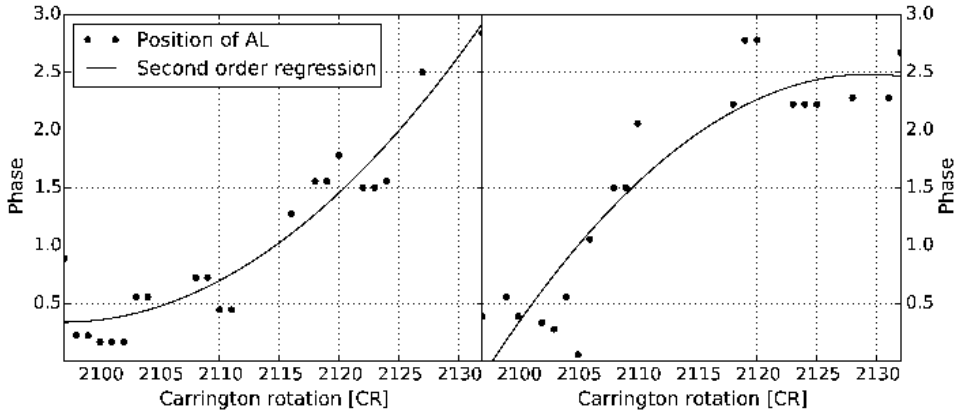

Fig. 4.2 The migration of the active longitudes in the time interval of CR 2097 to 2128 based on sunspot groups. The left panel sows the northern hemisphere. The right panel is the southern hemisphere.

at a specific longitudinal bin.

In each Carrington Rotation we omitted all of the $W_{i,CR}$ values which are lower than the 3σ significance limit. The highest peak, inferred as the active longitude in the Carrington Rotation co-ordinate frame, AL_{CR}, has been selected from this decayed sample (which contains only the significant peaks) caused by the significance test. For further analysis, the Carrington longitudes, λ, will now be transformed, into Carrington phase period:

$$\psi = \lambda / 360^{\circ}. \tag{4.3}$$

Hence, the values of the phases are always smaller or equal (which is the entire circumference) than one.

The time-variation of the parameter AL_{CR} is plotted in Figure 4.2. The vertical axis is the phase parameter, which has been repeated 3 times. The northern (left-hand-side) and the southern (right-hand-side) cases are considered separately. Both figures unveil a clear increasing migration pattern. Gyenge et al. (2014); Usoskin et al. (2005) found similar patterns at a different time interval. Most of the migration follows a parabola shape (which has been fitted by the least-square method).

4.4.2 Relationship between the AL and MS longitudinal distribution

The parameter $\delta\psi$ is now introduced to study the relationship between the active longitude, AL_{CR}, defined by sunspot groups, and the longitudinal position of MS

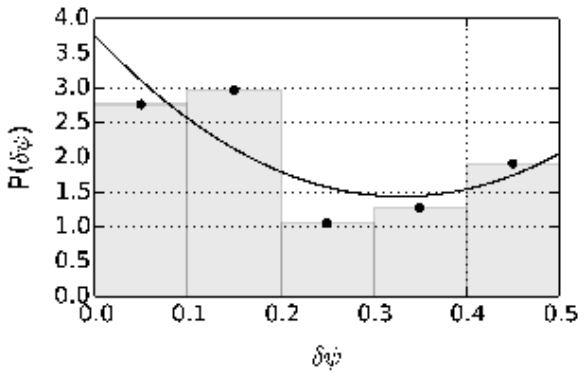

Fig. 4.3 Density distribution of the $\delta\psi$ parameter.

L_{CR} in Carrington Rotation co-ordinates.

$$\delta\psi = |AL_{CR} - L_{CR}|\,. \tag{4.4}$$

The parameter $\delta\psi$ has been reduced by a unit phase if it is larger than 0.5, which means this quantity represents the shortest phase difference between the longitudinal position of a given MS and the position of active longitudes in both hemispheres. Next, the $\delta\psi$ samples of the northern and southern hemispheres are now combined.

The probability density function (PDF) of the quantity $\delta\psi$ is shown in Figure 4.3. On the x-axis the meaning of the lower values reflect on the smallest longitudinal difference in phase, the value 0.5 phase jumps to the opposite side of the Sun.

The domain of interest of the quantity ϕ is $[-1;1]$. The $\phi = 0$ point contains the northern and southern poles. The $[0;1]$ sub-domain of ϕ represents the northern hemisphere, the ascending ϕ values from 0 to 1 show the descending latitudes from 90° to 0°. The southern hemispheres have been considered in the same way.

Figure 4.1 shows the result of the statistics above. The histogram depicts a normal distribution. $\overline{\phi} = 0.043$, this implies that most of the MS tend to cluster to the poles

The MS tend to cluster near the active longitudes, which is shown by the first and second peaks: $\delta\psi < 0.2(< \pm 36°)$ 61 % of the candidates. However, there is a significant peak around 0.5, which is the signature of the appearance of secondary longitudinal belts. The secondary belt exists alongside the primary belt temporally. It is always the case that the primary belt is always stronger than the secondary belt, as the name implies), and the phase shift is around 0.5. The MS show a similar behaviour, a secondary belt appears for 22% of the events and $\delta\psi < 0.1(< \pm 18°)$.

4.5 Summary

We investigated the distribution of MS detected at the solar surface as function of their longitudinal and latitudinal coordinates in Carrington co-ordinates.

A non-homogeneous latitudinal macrospicule distribution has been found. The macrospicules are found to have a non-homogeneous distribution in the Carrington co-ordinate frame. Most of the events tend to cluster to the higher latitudes (95% of MS are with in the $\pm 27^\circ$ to $\pm 90^\circ$ heliographic latitude). The number of the events is found to be growing exponentially from the equator to the pole in both hemispheres. A slightly asymmetrical behaviour has been found between the two hemispheres in the studied time interval, where the northern hemisphere was marginally more active than the southern.

The latitudinal spatial distribution of is not uniform either. A large proportion of the MS (83 of from the 101 in our sample) tend to cluster to the AL. In the case of the primary active longitude belt, the MS are within $\pm 36^\circ$ degrees of the active longitude. The secondary belt has a $\pm 18^\circ$ wide range within which the MS are found to be concentrated. This supports the existence of an active longitude at higher latitudes.

A large sample and more comprehensive statistical study is now in preparation for a more detailed search for further identifiable non-homogenous longitudinal distributions of MS in the entire time period covered by observations of the SDO satellite.

Chapter 5

A detailed case study of a jet-like feature at the limb

5.1 Introduction

Solar jets of various forms are ubiquitous throughout the solar atmosphere, from spicules and MS low in the chromosphere, both of which pass through the transition region, to coronal and X-Ray jets extending into the solar corona [Archontis and Török (2008); Madjarska (2011); Morton (2012)]. However, the lines between these features are still blurred, therefore in this chapter, I will examine, in detail, their formation and subsequent interaction with the solar atmosphere. Investigations into these phenomena have advanced significantly with recent developments in solar telescope technology, applied on missions like Hinode and the Solar Dynamics Observatory (SDO) and the most recent mission Interface Region Imaging Spectrometer (IRIS). Jet-like features are observed in a range of wavelengths, and therefore, heights in the atmosphere [Wang (1998); Yamauchi et al. (2004)]. With the instrumentation available to us, a similar treatment will be given to this feature.

Macrospicules are generally accepted as multi-thermal structures, featuring a cool core and a hot sheath resulting from formation in the cooler atmosphere, from being observed in Hα (Labonte, 1979) and hotter high chromosphere lines such as in Parenti et al. (2002). They have also been observed to rotate, Pike and Mason (1998) and Kamio et al. (2010), the latter paper quotes -120 ± 15 kms^{-1} blue-shifted Doppler velocity on the left side of the macrospicule.

There are multiple proposals for the mechanism triggering apparent rotation of the macrospicule. Curdt and Tian (2011) propose that the Sun's differential rotation causes MS rotation, whereas, reconnection events cause the relaxation of a small-scale twisted loop, as demonstrated by Adams et al. (2014). Again, with MS

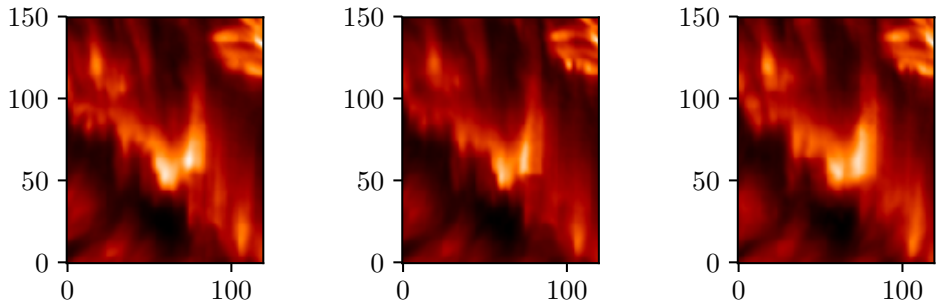

(a) (b) (c)

Fig. 5.1 a) Examine the two bright points in the proximity of (79",60"). The point on the left is significantly brighter than the fainter on the right. We emphasise that the brightening around (60",50") is not a contributor to this jet. b) In this frame the bright points have extended, the fainter point has now extended up to 95" and the core of the brighter left feature has grown with it. c) At this point the two separate points are now indistinguishable and the feature is now extending as one column.

extending high into the atmosphere, the question of their effect upon it, is one that needs answering. Pike and Harrison (1997) observe outflows from the MS of the order 200 kms^{-1} in He I and discuss whether these outflows could potentially accelerate the solar wind. However, work by Zaqarashvili et al. (2014) questions whether jets moving at super-Alfvénic speeds might cause a Kelvin-Helmholtz instability to form at the macrospicule/atmosphere boundary, which would, in turn, transport heat into the corona.

Kamio et al. (2010) applied a great deal of the background above when studying a macrospicule and X-Ray jet forming simultaneously. There is also discussion in Pike and Harrison (1997) and Kim et al. (2007) on the appearance of X-Ray jets, alongside small scale jets.

In the following sections we comprehensively discuss the physical properties of a case study. In Section 5.2 we present the observations we are using. 5.3 discusses the evolution of the jet with respect to its extent and the different view of the feature utilising STEREO-A's EUVI. Then move on to a doppler analysis of the jet in Section 5.4. Lastly, attempt to quantify the effect of the jet on the atmosphere in Section 5.5 before making our conclusions.

5.2 Observations

We observed a jet-like feature at the limb on 21st June 2016 beginning at 07 : 30 : 00 UTC in CRISP, an instrument installed on the Swedish Solar Telescope (SST)

during a period of good seeing, [Scharmer et al. (2003)]. We used the Hα filter, core line 656.28 nm with 35 slit increments from the core covering a .32 nm range, −0.2 nm and +0.12 nm, further processed using te Multi-Object Multi-Frame Blind Deconvolution (MOMBFD van Noort et al. (2005)). The observations were of Active Region 11506 with $xc = 893"$, $yc = -250"$ in heliographic coordinates on 930×930 pixel images, with spatial resolution of 0.012 arcsec/pixel and temporal resolution of 7.5 sec. Due to the range of solar observational platforms available to us, we also have simultaneous observations with the Solar Dynamic Observatory (SDO) and the Solar Terrestrial Relations Observatory (STEREO).

Using the Atmospheric Imaging Assembly (AIA), we observe the jet in most of the wavelengths available, 30.4, 35.5, 211, 17.1 and 13.1 nm. AIA on-board SDO (Lemen et al. (2012)) provides 4096×4096 pixel images with a spatial resolution of 0.6 arcsec per pixel and a cadence of 12 sec.

Lastly, we also have observations in STEREO using the Extreme Ultra Violet Imager (EUVI) [Defise et al. (2001)]. We are fortunate that when these observations were taken, STEREO A was at approximately 90° to the Sun-Earth line, as such we also have observations of this feature as an on-disk feature. In this case we are using the 30.4 nm HI instrument, however, the distance from the Earth has now reached a point that the temporal cadence has reduced to 10 min. While this is possibly too high to undertake a detailed examination, we can certainly utilise this method to inform us as to the global behaviour of the macrospicule. As we have a suite of observing instruments to utilise we aim to build a comprehensive description of this feature and how it may affect the environment around it.

5.3 Time-Distance Evolution

Let us begin with the evolution of the jet over time. We have utilised a self-built, manual, feature measuring tool, which uses a clicking mechanism to select the foot and tip of the macrospicule, calculates the half height and uses this as a guide to measure the width of the feature. Using this tool on each frame, and therefore the time cadence of the instrument, we obtain the evolution of the jet and general ballistic information. We have used this tool on each wavelength to examine the extent upwards through the corona. Observations in SDO record the entire lifetime of the feature, however the same is not true for observations using the SST, where the observation window in SST closes at 07 : 55 : 00 UTC.

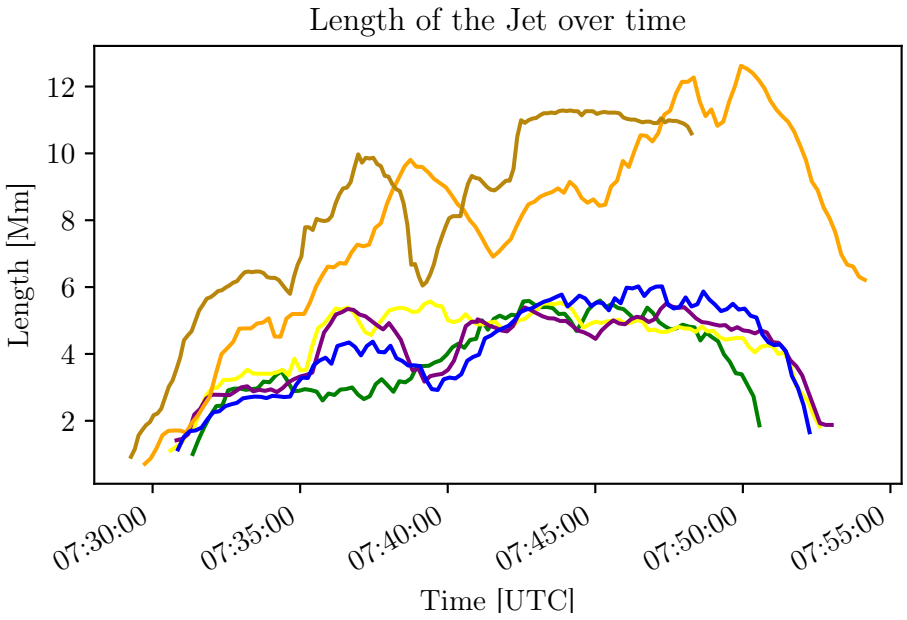

(a)

Wavelength (nm)	Maximum Length (Mm)	Maximum Velocity (km/s)
656.2	11.3	0.09
30.4	12.6	31.5
33.5	6.0	53.6
21.1	5.5	50.1
17.1	5.6	51.9
13.1	5.6	36.6

(b)

Fig. 5.2 a) Darkgold = Hα, Blue = 33.5 nm, Orange = 30.4 nm, Purple = 21.1 nm, Yellow = 17.1 nm, Green = 13.1 nm. The CRISP observations end earlier than the whole evolution of the jet, and the top of the jet is cut off by the top of the image. Therefore we ignore flatline at the top of the Hα line starting at 07 : 42 UTC. b) Table of maximised basic spatial properties of the jet.

5.3.1 Onset

The jet feature is observed as it forms using SST and, fortunately, we can resolve initial stages of the jet formation. The jet is observed to initiate in the core of Hα with two small bright points forming, and an ensuing jet developing above it. Figure 5.1 captures the early evolution of the jet in detail. Evident in Figure 5.1a we find the initial two bright points at the foot of the jet, the bright point of the left being significantly brighter than its countpart on the right. By Figure 5.1b shows the development of these two points *i.e.* have now become two columns of brighter

plasma. In the final formation stage, Figure 5.1c the jet has formed and is now a distinct feature against the background. This behaviour is in keeping with the standard jet formation model demonstrated by Shibata et al. (1992), where the authors describe an 'inverted y' shape of brightened material that is a result of small scale flux emergence reconnection.

5.3.2 Evolution

Let us examine the raw evolution of the jet in the time distance plot in Figure 5.2a. Here we have utilised the measuring tool to measure the extent of the feature in all the wavelengths in which it is visible. We find that the overall profile of its evolution contains two distinct peaks in most wavelengths, with the exception of 17.1 nm. The first peak comes at 07 : 37 UTC before a decrease in size and subsequent secondary expansion to its maximum length in Hα and 30.4 nm at approximately 07 : 49 UTC. This strongly implies that there is a second initialising type event in which a new material is accelerated into the atmosphere. As such let us turn to the CRISP instrument again.

With its higher resolution, a slit based analysis of the jet can be observed in Figure 5.3. Notice two distinct curves in the image, the first onset is at approximately 131 s and the second at a bright point originating at 655 s. We find that in this second phase of the jet, plasma extends higher into the atmosphere. This result is unusual as previous observations of recurrent jets have shown decay in subsequent initialisation events in observations such as Jiang et al. (2007). Unfortunately, a section of material is in front of the base of the jet and obscures our view of the second event.

Considering the observations in multiple wavelengths, we notice the smaller extension visible in the coronal wavelengths. In these higher temperature lines, the jet appears as a dark line. The appearance could be due to the fact that the feature is cool and cannot be observed at higher temperatures. However, when observed in SDO/AIA 30.4 nm, the feature appears dark over the limb and emissive beyond it. Observing the feature in EUVI, the feature appears entirely dark with bright foot points. Therefore, we cannot state that there is no emission at higher temperatures. However, this does allow us to categorise the jet as a feature of the chromosphere.

Evidently, the maximum extent of this feature is in He II 30.4 nm and maximises at 12.6 Mm although the measurements in Hα may exceed this were it to be fully visible. Interestingly, the length of the jet in the coronal lines does not get larger after the second injection on plasma occurs. This subsequent acceleration of plasma originates from the same location as that of the initial formation, and on the same

scale as the first onset. However, this drives the tip of the jet even higher than the initial tip, measuring the velocity accurately is difficult, due to this acceleration is set against the previous bright material. An approximation using multiple image steps and using a difference delta produces an average of 46 km s^{-1}, therefore we can infer that it reaches a higher maximum velocity than the first ejection.

The feature is very thin, averaging 1.13 Mm in Hα and 0.787 Mm in He II. This result is unexpected, it certainly seems to contradict the cool core surrounded by a hot sheath model. However the errors on the measurement in SDO/AIA recordings are ±1.5 Mm, when taking into account human measurement error and resolution of the instrument. Where as measurement error on the SST/CRISP images is ±0.0885 Mm, thus, we are more inclined to believe the measurement according to CRISP. This thin spire is an expected outcome of the standard model of jet formation, more on which later.

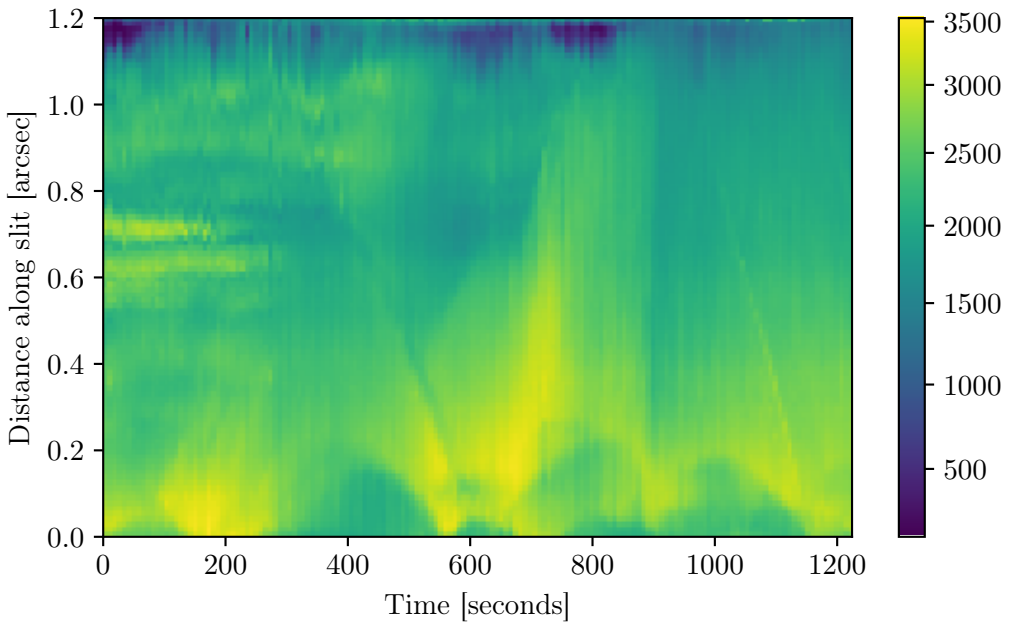

Fig. 5.3 SST/CRISP Hα line core time-distance diagram along the centre of the jet spire.

5.3.3 STEREO-A

Next, consider the observations in EUVI, with the instrument positioned at 90° to the Sun-Earth line. This facilitates the building of a larger picture of the behaviour of the jet, the downside to this however, is that with STEREO-A being at such a distance the cadence is low, 10 mins. In this case we obtain 4 images in 30.4 nm in

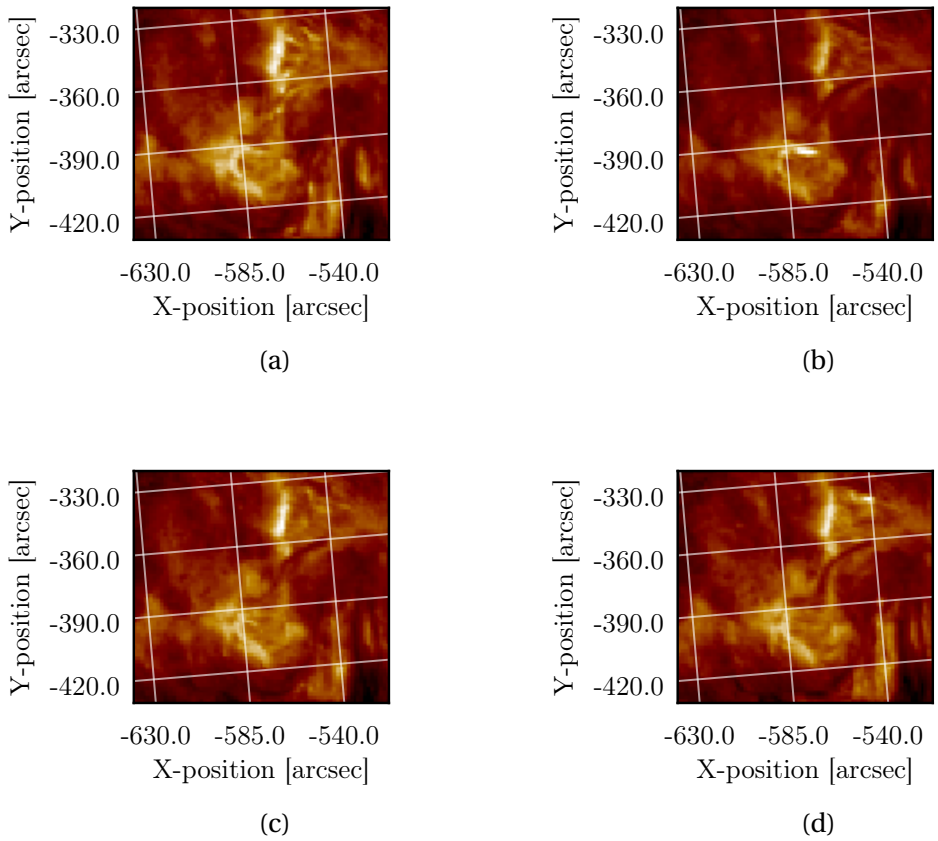

Fig. 5.4 EUVI 30.4 nm images from STEREO on 21st June at a) 07 : 26 : 15 UTC, b) 07 : 36 : 15 UTC, c) 07 : 46 : 15 UTC and d) 07 : 56 : 15 UTC.

which the jet is observed. The jet appears as a dark fibril like feature originating at approximately $-570''$ to $-385''$ longitude , and extending across the disk to a length of 45.1 arcsec. Significantly, the component of extension in the East-West direction is not insignificant, approximately 30 arcsec. With this information we calculate that the total length of the feature, taking into account both SDO and STEREO's view, is 25.5 Mm.

5.4 Doppler Shift

Possibly the most valuable information to be gained about the development of jets, is pertaining to it rotational behaviour, therefore, we will use the spectral increments from the CRISP instrument to obtain line-of-sight Doppler velocities. There is, however, a hindrance with this. There are two separate forms of the emission spectra within the image. The region where the jet initialises, is on disk, and as a result the

spectral analysis reveals an absorption spectra.

5.4.1 MCMC Method

We have developed this algorithm to address this particular problem, using the overall shift of the emission line from the standard emission. Over the limb, however, the spectral profile changes to emission and we find two peaks. As a consequence of this, finding the total shift away from the core, 656.28 nm, is made more complex. For pixel points which are on-disk, we fit a single Gaussian and calculate the minima, as is standard, and for the two peak spectra, we have utilised a double Gaussian, finding the minima between the two. However, the problem becomes evident when we need to change between the two routines.

We have utilised a Markov Chain Monte Carlo (MCMC) (Richey (2010)) method to find the most accurate fit and the Bayesian Information Criterion (BIC) to test which of the two fits is most appropriate from a given line as a solution to this problem.

This method takes the 35 spectral intensity for a given pixel and samples multiple possible fits for the profile these produce. We then find the most likely fit from this range and minimise this final fit to find the mean value of the fit. Difference between the original core value and mean of the new fit is the calculated shift in wavelength, and therefore, the line-of-sight velocity for the chromospheric plasma. The process is the same for both single and double Gaussian fitting and as such we apply a BIC to test which fit is more appropriate. BIC has limitations when the number of parameters is of the same order of the size of the sample and differentiating between multiple complex models. In this case the sample is larger than the number of parameters and we are only testing two possible models, as such, we can use the test with confidence in the results.

The result of applying the above method to the SST/CRISP spectroscopic dataset is presented in Figure 5.5. Immediately apparent, is the banding structured red and blue shifts, the effect is created as a result of the optical depth created when observing at the limb. The jet forms in amongst a cluster of blue-shifted smaller thin structures, making early observations in the dopplergrams difficult.

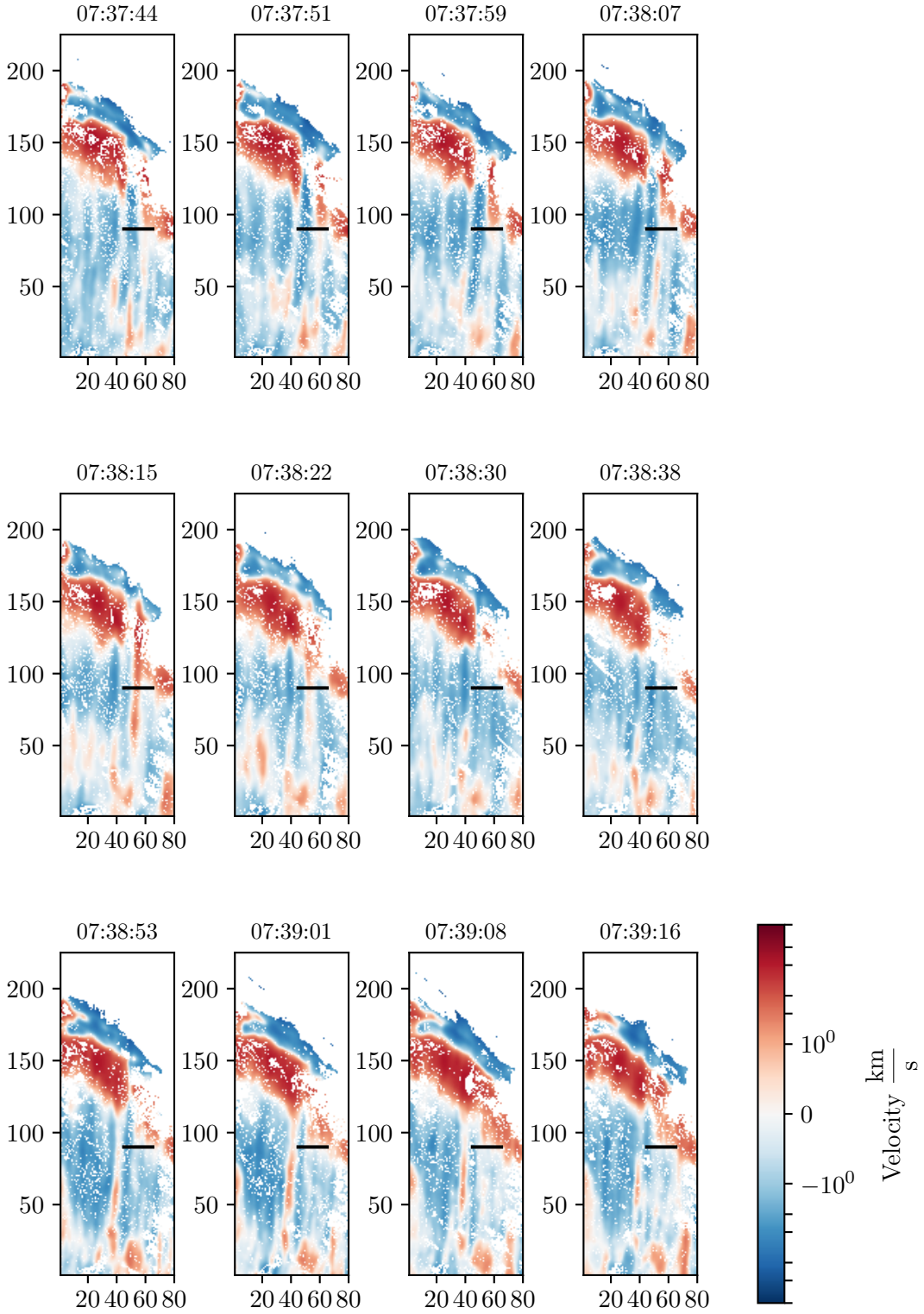

Fig. 5.5 Above is the result of the dopplergram processing during the evolution of the second ejection of plasma starting at 07 : 37 : 00 UTC. All images shown in pixel coordinates.

5.4.2 Analysis

This particular feature, as has already been mentioned, has two events in which material is accelerated upwards into the solar atmosphere. The first event is not readily visible in the dopplergrams, difficult as it is to pick out against a line of spicule-like features all showing blue-shifts, towards the viewewing direction. This result is to be expected given the we have demonstrated movement away from the 'camera' in Figure 5.4. Whereas, the second expulsion of material, originating at 07 : 37 UTC, exhibits the classic behaviour of a rotating feature in dopplergrams, a red/blue split over the body of the feature.

It is clear that the second event comes from a similarly small element to the first and evolves upwards, joining the full formation of the jet, hence why the apparent rotation of the jet does not appear to spread across the rest of the jet as seen in Hα.

As the jet evolves we see an initial blue-shift, matching the acceleration upwards seen in Hα, and it is only after a few second seconds of evolution that rotational behaviour begins to become evident. The first panel in Figure 5.5 at 07 : 37 : 44 UTC demonstrates the first panel where there might be in inkling of red-shift on the right ride of the feature, with a thin line registering as moving away from the camera. Noticeably, this rotation does not begin at the base of the feature, instead, the rotation manifests from the tip downwards over the next two images at 07 : 37 : 51 UTC and 07 : 37 : 59 UTC.

By the time the jet reaches 07 : 39 : 07 UTC, we begin to observe a thin formation of red-shift at the right side of the base of the feature, subsequently by 07 : 38 : 15 UTC, the red-shift has entirely taken over the right hand side. Though once again, the next frame shows progression up the spire of the feature.

We subsequently observe the sift to disappear from the right hand side of the jet, however, the subsequent two images show an element of red-shift now on the left of the feature. This element consequently develops into longer feature in 07 : 38 : 53 UTC and subsequent images, to the point where red-shift now dominates the left hand side of the feature.

This is a result of the magnetic pressure acting as restoring force, and rotating the feature in the opposite direction. However in this case, not to the same magnitude, an expected outcome due to inherent loss of energy from the system. By the last panel at 07 : 39 : 16 UTC, the feature has returned to a 'neutral' state, as such we can estimate an approximate period of a minute and a half.

This behaviour is extremely interesting as it demonstrates a torsional motion of the entire body of the feature, with the structure rotating anti-clockwise and then clockwise. This is a result of the release of magnetic tension in the initial reconnec-

tion event causing an unwinding of the inherent twist in the initial loop. We suggest that, as a result of the speed of the initial acceleration of the plasma material, this untwisting began at the top of the plasma column as is seen in 07 : 37 : 51 UTC. The peak of this untwisting, when the red-shift dominates the RHS at 07 : 38 : 15 UTC, with the highest velocity values observed at approximately $3-4$ km s^{-1} and the 'body' of the feature demonstrating velocities in the range $1.0-1.5$ km 9s^{-1}.

The velocity values given here are slow compared to those presented in previous works, however, we believe these to be accurate, and attribute this to the smalls scale of the initial loop. A larger scale loop would mean that the magnetic tension would be greater, and hence, experience greater restoring force, inducing higher velocities.

5.5 Effect on the atmosphere

With the increased resolution we can visually inspect the boundary between the jet and atmosphere. Figure 5.6 details the evolution of the jet in the core of Hα in over 115 seconds. At the boundary we observe narrow dark columns in the emission on either side of the jet. Given that they appear on either side of the jet column and that the observations are in the core of the $H\alpha$ line, it is unlikely that this would be caused by a Doppler-like effect. One possibility is that the cause is an instability effect, such as shear or Kelvin-Helmholtz, seen in Zaqarashvili et al. (2014) as the jet moves throughout the higher atmosphere. Supporting this hypothesis is that these images were recorded in the 'second phase' of the jet *i.e.* after the second reconnection and the jet extends to its peak in He II 30.4 nm. As such, it is possible that these columns are a result of plasma being accelerated through the less dense atmosphere.

One of the possible primary results of these instabilities is a dissipation of energy into the surrounding atmosphere, as such we might expect an increase in temperature of the surrounding atmosphere. To this end we will utilise the temperature calculation method highlighted in Leonard and Morgan (2014).

The authors use a Differential Emission Measure (DEM) to obtain a temperature response from the SDO/AIA measurements. The temperature response is a combination of the wavelength response from the instrument and the contribution function which describes the emission from a given temperature. When using such a scheme, we need to decide on a general DEM profile to be applied to all pixels. The method uses a Gaussian scan across the emission in each line and property of the Gaussian; mean, amplitude and width. Utilising a narrow Gaussian seems to provide the most accurate values when compared to synthetic observations.

Figure 5.7 demonstrates the behavioural change of the temperature across the

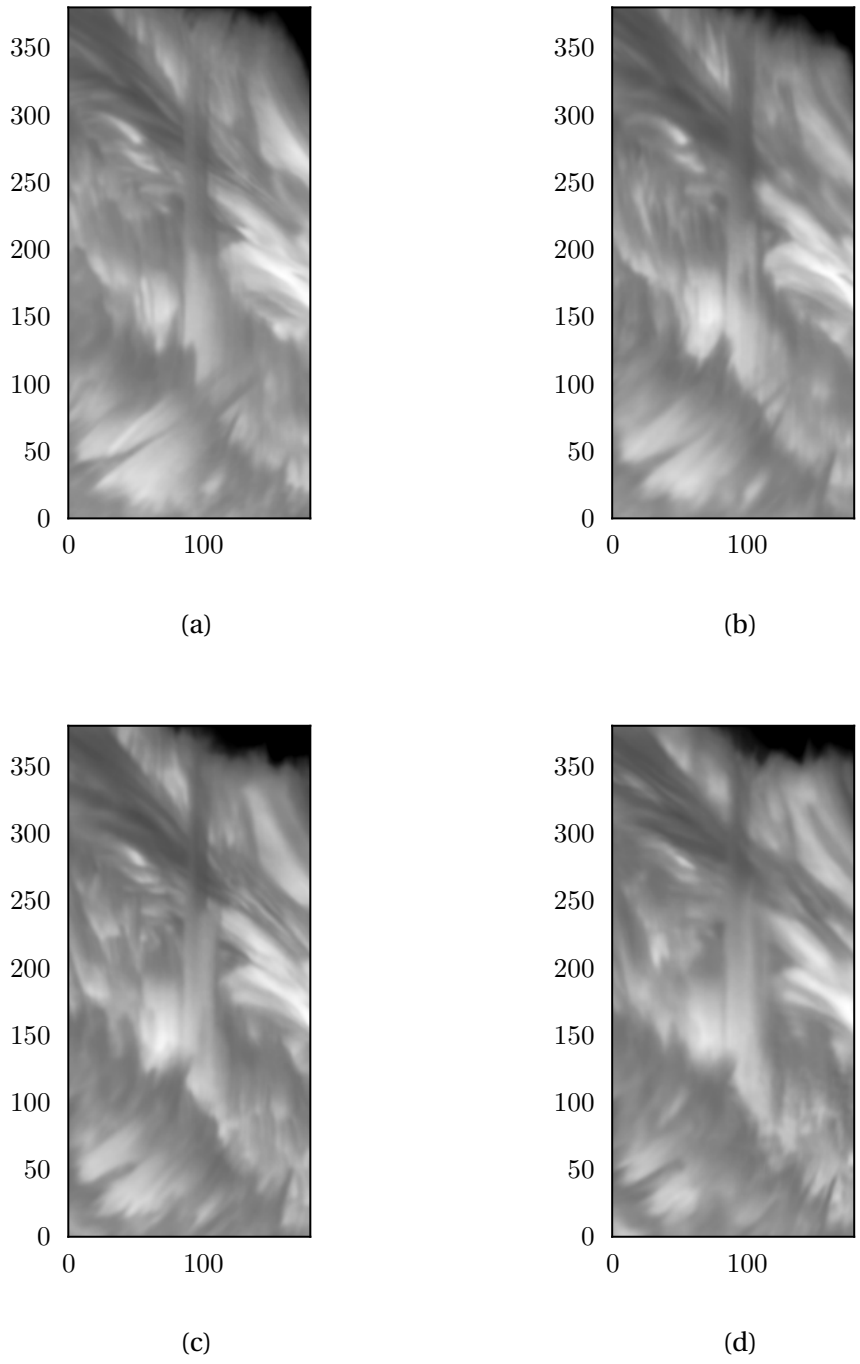

Fig. 5.6 Sequence of images detailing an intermediate phase of the jets evolution. Beginning with a) 07:36:19 UTC, b) 07:36:19 UTC, c) 07:37:36 UTC and d) 07:38:15 UTC

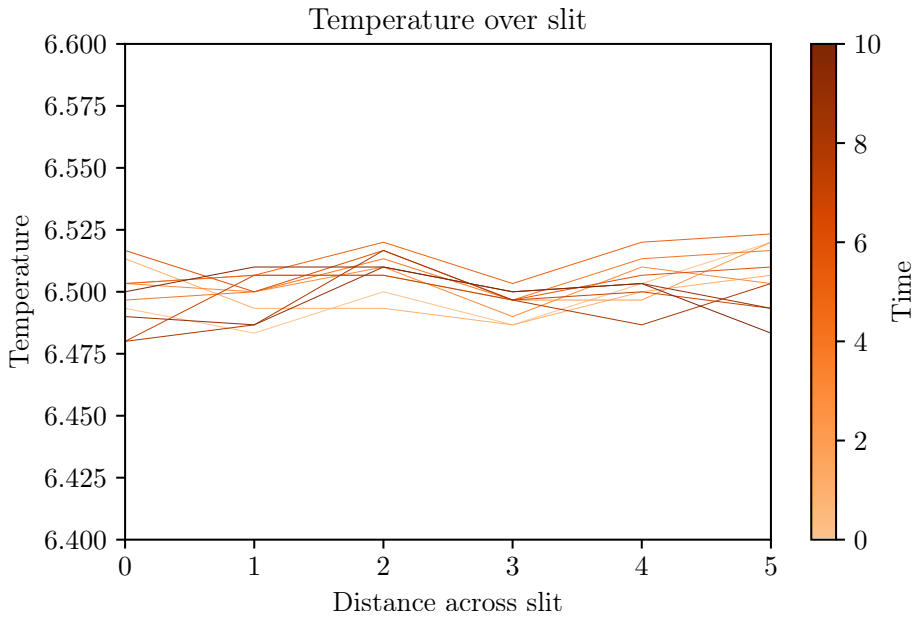

Fig. 5.7 The AIA maps were processed into temperature maps, and a slit was taken at the half height, perpendicular to the axis of evolution. The temperature maps were taken for the time over which the second acceleration of material occured. The colorbar indicates the passage of time and the various lines applicable to the slits is demonstrated.

normal of the feature by slit based analysis. By performing this analysis over the time domain of the second ejection of plasma material, we will acertain whether the feature has any impact on the atmosphere. The difficulty with this form if measurement is that the feature itself is not particularly wide, 1 Mm, and therefore is has only one or two pixels of actual jet material for us to examine. The jet is located around the 3rd and 4th pixels of the x axis, and as we would expect we see a moderate dip, when compared to the surroundings. Noticeable as well, however, is that at what is approximately the boundaries, there is a peak in temperature, before it drops as distance increases with respect to the jet.

These values are not conclusive, we require temperature maps on a much finer spatial scale, and as well, new techniques to develop to overcome the problems of the extremely broad Hα and He II lines causing a blurring of possible values. However, in conjunction with the observations presented here of possible shearing or Kelvin Helmholtz instability causing a lack of emission at the boundary of the jet, we can present the hypothesis more confidently. In terms of the bigger picture in which spicules/jets/MS contribute to heating of the solar corona, the results produced by this feature are not typical. With respect to other studies, this feature cannot be considered that quick, or large, or excessively rotational, yet it may be

having a measurable effect. Hence, applying this kind of comprehensive analysis to multiple jets, particularly rapidly evolving examples, to ascertain their impact on the atmosphere fully is the next area of investigation for these jets. An endeavour which will be aided significantly by the operation commencement of DKIST, with its superior everything.

5.6 Discussion & Conclusion

We observe a jet-like feature at the solar limb on 21st June 2012 at 07 : 30 : 00 UTC on the solar limb, centred at 910, 234 solar helioprojective co-ordinates. We have multiple methods with which to view the feature, SST/CRISP, the range of SDO/AIA coronal wavelengths and STEREO-A/SECCHI. We have utilised multiple analysis techniques to build a comprehensive picture of the jet-like features motion and the possible impacts on the atmosphere above it.

From the observation of this feature, we can draw the following conclusions

- This particular feature is visible in Hα and He II 30.4 nm, and thus, is inherently a chromospheric object.
- The jet has two separate ejections of material. Reaching a maximum *length* of 25 Mm.
- The formation of the jet is observed to be similar to the standard jet formation mechanism.
- The jet has a rotational component to its motion.

The feature is observed to extend to 12.6 Mm in He II 30.4 nm (and is only found to be shorter in Hα due to moving out of the viewing field of view). Its lifetime is measured of to be 20 mins and radial velocities are found to be maximised during the initial acceleration, and are of the order $50-60$ km s^{-1} during the first acceleration of the feature. However the second acceleration of material proves awkward to measure accurately, however we estimate slightly higher maximum velocities, but similar averages over the extension upwards. This very much puts this feature in the category of MS, agreeing with the values presented in Chapter 3.

However the feature exhibits similar formation mechanisms as a standard jet following the pattern demonstrated in Shibata et al. (1992) and then built on by Moore et al. (2010), who also presented the blowout jet mechanism. With the two visible bright points in the Hα images which come to form an, all be it, long thin bright arch before forming the characteristic spire of a the standard jet. Unfortunatley, Hinode's

XRT instrument was in a power down mode during the formation of this feature and RHESSI did not record the event, as such, we are missing crucial X-Ray data.

If an increase in the X-Ray radiation were to be found, the question as to the categorisation of such a feature becomes important. Given that we observe several of the key indicators of a standard jet, could this not also be classified as a standard jet? Inspite of this features relatively small size, this could be classified as an X-Ray jet. However the question remains, is this a macrospicule? And if so, do we classify the feature as a macrospicule or a standard jet?

In answer to these questions, one possible differentiator is the appearance in the higher coronal wavelengths. In this case, the jet appears as an absorption feature, against the brighter limb. This does not mean that the jet does not reach coronal temperatures, in 30.4 nm the jet appears as absorption below the limb and as emission above it. We cannot conclusively say that the jet contributes to the coronal emission by visual inspection.

Therefore, we propose that this is a standard jet, and as a community, we need to fully address the underlying physics of MS. This is despite the ambiguity about its appearance in the coronal emission lines, but the underlying physics is enough to draw this conclusion.

The spectroscopic readings, as shown in Section 5.4, demonstrates a small, but appreciable perturbation in the rotational velocity of the jet like feature. We find that the jet exhibits a torsional behaviour, demonstrating shifts indicating rotation in one direction and then the other. The magnitude of these velocities is, however, low. we conclude that this is a result of the very small source loop of the feature, although this of course needs further enquiry.

With respect to the features affect on the atmosphere, we find a boundary interaction between the jet and atmosphere in the Hα images. This interaction has manifested as dark streaks at the every edges of the feature during the same phase in which the second event causes the acceleration of further plasma. It is also the phase in which we observe the torsional rotation of the jet. Whether these dark streaks are physically significant we cannot comment upon too confidently at this time, but they appear at the same time as the second acceleration and the onset of rotational behaviour, cannot merely be coincidence.

Chapter 6

Conclusions

Macrospicules are an intriguing feature of the solar atmosphere. The work that is presented in this thesis has attempted to shed some light on these prevalent parts of the atmosphere. Chapter 3 can be easily compared to the previous works on a like-for-like basis. The previous examples of measurements, given by Bohlin et al. (1975) and Dere et al. (1989), are compared in Table 3.2. The values found here compare particularly well with Bohlin, however, the work by Dere finds more conservative values. Given the improved nature of instrumentation and measuring tools utilised in this work, we assert that the values found here should become the new expected measurements defining a macrospicule.

This study also found no divergence in the population of features measured. Such an effect could be expected were MS very similar to another feature, but with separate underlying physics. Of course, the possibility remains that, they are part of a larger scale feature, such as X-Ray jets, which, has been discussed on multiple occasions, Kamio et al. (2010); Parenti et al. (2002). In these cases, the jet-like features' properties are similar to those of regular MS, but there is no evidence to support this hypothesis within this study.

With respect to the ballistics and energetics of the feature, we find the unexpected effect of a macrospicule becoming thinner as it falls down in the atmosphere. Another theory could be that the magnetic pressure would cause the width to increase, however the evidence does not agree with this, as such we need to think about the macrospicule not just as a column of regular plasma. The likely case is that the plasma begins to flow down the magnetic field lines, in a similar manner to evanescence, resulting in a decrease in the width of the feature.

Chapter 4 demonstrates that macrospicules' properties are dictated by larger processes in the Sun. That macrospicules tend to form along an active longitude is likely due to the influence of the tachocline. This result has subsequently been

given more credence as a result of the work undertaken by Kiss et al. (2017) finding a short term, 1 - 2 year cycle in macrospicule length. Again, this could be due to the influence of the tachocline dynamo effects creating the global magnetic field.

Chapter 5 presents the most comprehensive view of a macrospicule in this thesis. The most significant result, is demonstrated very clearly in the line of sight dopplergrams. The macrospicule feature clearly shows a rotation initially in the anti-clockwise direction, before slowing in rotation rate, stopping and then rotating clockwise. This is the first observation of such behaviour in a macrospicule. In contrast, there have been multiple observations and simulations of rotating jet-like features, *e.g.* Curdt and Tian (2011); Kamio et al. (2010); Madjarska (2011), however, this is the first work demonstrating torsional oscillating motion in either jet or macrospicules. It is also apparent that the observed 'unwinding' motion starts from the tip of the macrospicule before moving downwards. This unequivocally proves that MS have an intrinsic magnetic field. The presence of a magnetic field in the macrospicule constrains the formation mechanism, to those involving the simultaneous expulsion of plasma and magnetic field, which is highlighted in Section 1.2.2.

The resolution of SST allows us to examine the footpoint of the macrospicule. The conclusion that arises from this is that the macrospicule seems to undergo a formation event similar to the Shibata et al. (1992) standard jet formation model. The brightenings evident in the Hα line, show two much smaller brightpoints evolving and joining before the spire eventually forms. The extension of this feature in the lower temperature emission lines, where it extends the furthest, is roughly 12 Mm. We have therefore observed a small-scale feature with a very similar formation mechanism to larger coronal jets. This leads to the conclusion that macrospicules should perhaps be classified as standard jets. Given that this feature is very thin, but Chapter 3 shows average widths of the order of 7 Mm, therefore should the population be separated in terms of formation processes, i.e. standard and 'blowout' style MS, in the same way as jets?

Macrospicules and their relationship (or lack thereof) with jets, will continue to be essential to our understanding of the solar atmosphere, given that they originate in the low chromosphere and extend up into the corona. The questions of the most importance at the moment are of their structure and formation mechanism. Both of these may be answered by the new DKIST telescope. The leap forward that DKIST will take with respect to spatial and temporal resolution will allow us to examine the footpoints of these features with significantly greater accuracy. Possibly more intriguing is the body of MS themselves. Given the 'unwinding' of magnetic twist observed in Chapter 5, it may be possible to inspect individual strands of flux rope, which could answer:

- Are the MS unwinding in all cases?
- Could the twisting motion be a result of a driver from below?
- Do the MS always have a torsional or helical component?
- Can MS be considered as a major factor with respect to heating or solar wind acceleration?

Those are just the questions considering MS on their own. Macrospicules' current place in the plethora of jet-like solar features is still far from clear, despite this work. Are MS instances of multiple spicules 'superposing' and becoming a much larger feature as supposed by Xia et al. (2005)? Are they the cool component of X-Ray jets as in Parenti et al. (2002)? In which case should we merely be calling them X-Ray jets observed in chromospheric emission lines? There has been much work on the subject of Hα and He II 30.4 nm MS, including work by Labonte (1979); Wang (1998) but we have yet to conclusively prove that these features are one and the same. However, Chapter 5, again demonstrates that this is the case.

The future of the study of MS lies with observations. At the moment, there is no shortage of models sufficiently complex to describe, in detail, the method by which macrospicules are formed, authors such as Murawski et al. (2011), Archontis et al. (2005) and Moreno-Insertis et al. (2008) have covered his extensively. What is required is tuning of the initial conditions and magnetic configuration at the time of onset.

This is now possible with the building of DKIST. DKIST will be the most advanced telescope of the current age of solar observations, with a 4 meter mirror it will be able to resolve 10 km on the solar surface and a very high temporal cadence, it can be pushed as low as 1/3 of a second [Woeger (2016)]. With this instrument, we will be able to record the moment that a macrospicule is formed in extreme detail. The most efficient way, given macrospicules infrequency compared to spicules, would be to focus attention to the coronal hole boundaries given that 20% of macrospiules are formed there, Chapter 3, and the area too cover is much smaller than the alternative coronal holes and quiet Sun.

Over a large sample window, collecting as many MS evolution as possible, would allow a statistical distribution of the rotational velocities of the macrospicules to be found. Testing whether the rotational velocity measured in Chapter 5 is the expected value or overly slow. This will have an impact going forward as it would demonstrate whether the Kelvin-Helmholtz instability [Zaqarashvili et al. (2014)] could heat the corona through the volume of spicules/macrospicules in the chromosphere.

However, the most import subject with respect to macrospicules is their classification among the solar jets. Chapter 5 demonstrates that a feature with similar size and dimension to those in Chapter 3 can have formation patterns equatable to much larger features such as X-Ray and EUV jets. As the study of jets carries forward, the question at the front the solar physicist's mind should be, are jets observed in the lower temperatures actually different features to hotter jets, or just their footprint lower in the atmosphere?

References

Adams, M., Sterling, A. C., Moore, R. L., and Gary, G. A. (2014). A Small-scale Eruption Leading to a Blowout Macrospicule Jet in an On-disk Coronal Hole. , 783:11.

Alfvén, H. (1942). Existence of Electromagnetic-Hydrodynamic Waves. , 150:405–406.

Antiochos, S. K. (1998). The Magnetic Topology of Solar Eruptions. , 502:L181–L184.

Archontis, V., Moreno-Insertis, F., Galsgaard, K., and Hood, A. W. (2005). The Three-dimensional Interaction between Emerging Magnetic Flux and a Large-Scale Coronal Field: Reconnection, Current Sheets, and Jets. , 635:1299–1318.

Archontis, V. and Török, T. (2008). Eruption of magnetic flux ropes during flux emergence. , 492:L35–L38.

Aschwanden, M. J., Winebarger, A., Tsiklauri, D., and Peter, H. (2007). The Coronal Heating Paradox. , 659:1673–1681.

Athay, R. (2000). Are spicules related to coronal heating? *Solar Physics*, 197(1):31–42.

Athay, R. G. and Beckers, J. M. (1976). The Solar Chromosphere and Corona: Quiet Sun. *Physics Today*, 29:74.

Balthasar, H. and Schüssler, M. (1984). Evidence for the 22-YEAR-CYCLE in the Longitudinal Distribution of Sunspots. , 93:177–179.

Beckers, J. M. (1972). Solar Spicules. , 10:73.

Benevolenskaya, E. E., Kosovichev, A. G., and Scherrer, P. H. (1999). Structure and Dynamics of Interconnecting Loops and Coronal Holes in Active Longitudes. , 190:145–151.

Bennett, S. M. and Erdélyi, R. (2015). On the Statistics of Macrospicules. , 808:135.

Bohlin, J. D., Vogel, S. N., Purcell, J. D., Sheeley, Jr., N. R., Tousey, R., and Vanhoosier, M. E. (1975). A newly observed solar feature - Macrospicules in He II 304 A. , 197:L133–L135.

Brun, A. S. (2001). The solar tachocline: Where do we stand? In Wilson, A. and Pallé, P. L., editors, *SOHO 10/GONG 2000 Workshop: Helio- and Asteroseismology at the Dawn of the Millennium*, volume 464 of *ESA Special Publication*, pages 273–276.

Bumba, V. and Howard, R. (1965). A Study of the Development of Active Regions on the Sun. , 141:1492.

Chaplin, W. J. (2014). *Sounding the solar cycle with helioseismology: Implications for asteroseismology*, page 1.

Chidambara Aiyar, P. R. (1932). Two longitudinal zones of apparent inhibition of sunspots on the solar disc. , 93:150.

Cirtain, J. W., Golub, L., Lundquist, L., van Ballegooijen, A., Savcheva, A., Shimojo, M., DeLuca, E., Tsuneta, S., Sakao, T., Reeves, K., Weber, M., Kano, R., Narukage, N., and Shibasaki, K. (2007). Evidence for Alfvén Waves in Solar X-ray Jets. *Science*, 318:1580.

Cranmer, S. R. (2009). Coronal Holes. *Living Reviews in Solar Physics*, 6.

Curdt, W. and Tian, H. (2011). Spectroscopic evidence for helicity in explosive events. , 532:L9.

De Pontieu, B., Erdélyi, R., and James, S. P. (2004). Solar chromospheric spicules from the leakage of photospheric oscillations and flows. , 430:536–539.

De Pontieu, B., Hansteen, V. H., Rouppe van der Voort, L., van Noort, M., and Carlsson, M. (2007a). Observations and Simulations of Fibrils and Mottles. *ArXiv Astrophysics e-prints*.

De Pontieu, B., McIntosh, S., Hansteen, V. H., Carlsson, M., Schrijver, C. J., Tarbell, T. D., Title, A. M., Shine, R. A., Suematsu, Y., Tsuneta, S., Katsukawa, Y., Ichimoto, K., Shimizu, T., and Nagata, S. (2007b). A Tale of Two Spicules: The Impact of Spicules on the Magnetic Chromosphere. , 59:S655–S662.

Defise, J.-M., Halain, J.-P., Mazy, E., Rochus, P. P., Howard, R. A., Moses, J. D., Socker, D. G., Simnett, G. M., and Webb, D. F. (2001). Design of the Heliospheric Imager for the STEREO mission. In Siegmund, O. H., Fineschi, S., and Gummin, M. A., editors, *UV/EUV and Visible Space Instrumentation for Astronomy and Solar Physics*, volume 4498 of , pages 63–72.

Dere, K. P., Bartoe, J.-D. F., Brueckner, G. E., Cook, J. W., and Socker, D. G. (1989). UV observations of macrospicules at the solar limb. , 119:55–63.

Feng, L., Inhester, B., de Patoul, J., Wiegelmann, T., and Gan, W. Q. (2012). Particle kinetic analysis of a polar jet from SECCHI COR data. , 538:A34.

Fleck, B. and Müller, D. (2016). 20 Years of SOHO. *Europhysics News*, 47(3):27–31.

Fleck, B., Müller, D., Haugan, S., Sánchez Duarte, L., Siili, T., and Gurman, J. B. (2006). 10 years of SOHO. *ESA Bulletin*, 126:24–32.

Goedbloed, J. P. H. and Poedts, S. (2004). *Principles of Magnetohydrodynamics*.

Golub, L. and Pasachoff, J. M. (2009). *The Solar Corona*.

Gyenge, N., Baranyi, T., and Ludmány, A. (2012). Distribution of activity at the solar active longitudes between 1979 - 2011 in the northern hemisphere. *Central European Astrophysical Bulletin*, 36:9–16.

Gyenge, N., Baranyi, T., and Ludmány, A. (2014). Migration and Extension of Solar Active Longitudinal Zones. , 289:579–591.

Gyenge, N., Bennett, S., and Erdélyi, R. (2015). Non-homogeneous Behaviour of the Spatial Distribution of Macrospicules. *Journal of Astrophysics and Astronomy*, 36:103–109.

Győri, L., Baranyi, T., and Ludmány, A. (2011). Photospheric data programs at the Debrecen Observatory. In Prasad Choudhary, D. and Strassmeier, K. G., editors, *Physics of Sun and Star Spots*, volume 273 of *IAU Symposium*, pages 403–407.

Habbal, S. R. and Gonzalez, R. D. (1991). First observations of microspicules at 4.8 GHz at the solar limb in polar coronal holes. , 376:L25–L27.

Heggland, L., De Pontieu, B., and Hansteen, V. H. (2009). Observational Signatures of Simulated Reconnection Events in the Solar Chromosphere and Transition Region. , 702:1–18.

Hertzsprung, E. (1909). Über die Sterne der Unterabteilungen c und ac nach der Spektralklassifikation von Antonia C. Maury. *Astronomische Nachrichten*, 179:373.

Hollweg, J. V. (1982). On the origin of solar spicules. , 257:345–353.

Isobe, H., Proctor, M. R. E., and Weiss, N. O. (2008). Convection-driven Emergence of Small-Scale Magnetic Fields and their Role in Coronal Heating and Solar Wind Acceleration. , 679:L57–L60.

Jiang, Y. C., Chen, H. D., Li, K. J., Shen, Y. D., and Yang, L. H. (2007). The Hα surges and EUV jets from magnetic flux emergences and cancellations. , 469:331–337.

Kaiser, M. L., Kucera, T. A., Davila, J. M., St. Cyr, O. C., Guhathakurta, M., and Christian, E. (2008). The STEREO Mission: An Introduction. , 136:5–16.

Kamio, S., Curdt, W., Teriaca, L., Inhester, B., and Solanki, S. K. (2010). Observations of a rotating macrospicule associated with an X-ray jet. , 510:L1.

Kayshap, P., Srivastava, A. K., Murawski, K., and Tripathi, D. (2013). Origin of Macrospicule and Jet in Polar Corona by a Small-scale Kinked Flux Tube. , 770:L3.

Kim, Y.-H., Moon, Y.-J., Park, Y.-D., Sakurai, T., Chae, J., Cho, K. S., and Bong, S.-C. (2007). Small-Scale X-Ray/EUV Jets Seen in Hinode XRT and TRACE. , 59:S763–S769.

Kiss, T. S., Gyenge, N., and Erdelyi, R. (2017). Quasi-biennial oscillations in the cross-correlation of properties of macrospicules. *ArXiv e-prints*.

Klimchuk, J. A. (2012). The role of type II spicules in the upper solar atmosphere. *Journal of Geophysical Research (Space Physics)*, 117:A12102.

Kudoh, T. and Shibata, K. (1999). Alfvén wave model of spicules and coronal heating. *The Astrophysical Journal*, 514(1):493.

Kuridze, D., Henriques, V., Mathioudakis, M., Erdélyi, R., Zaqarashvili, T. V., Shelyag, S., Keys, P. H., and Keenan, F. P. (2015). The Dynamics of Rapid Redshifted and Blueshifted Excursions in the Solar Hα Line. , 802:26.

Labonte, B. J. (1979). Activity in the quiet sun. I - Observations of macrospicules in H-alpha and D3. , 61:283–296.

Lang, K. R. (2009). *The Sun from Space*.

Lee, D. and Deane, A. E. (2009). An unsplit staggered mesh scheme for multidimensional magnetohydrodynamics. *Journal of Computational Physics*, 228:952–975.

Lemen, J. R., Title, A. M., Akin, D. J., Boerner, P. F., Chou, C., Drake, J. F., Duncan, D. W., Edwards, C. G., Friedlaender, F. M., Heyman, G. F., Hurlburt, N. E., Katz, N. L., Kushner, G. D., Levay, M., Lindgren, R. W., Mathur, D. P., McFeaters, E. L., Mitchell, S., Rehse, R. A., Schrijver, C. J., Springer, L. A., Stern, R. A., Tarbell, T. D., Wuelser, J.-P., Wolfson, C. J., Yanari, C., Bookbinder, J. A., Cheimets, P. N., Caldwell, D., Deluca, E. E., Gates, R., Golub, L., Park, S., Podgorski, W. A., Bush, R. I., Scherrer, P. H., Gummin, M. A., Smith, P., Auker, G., Jerram, P., Pool, P., Soufli, R., Windt, D. L., Beardsley, S., Clapp, M., Lang, J., and Waltham, N. (2012). The atmospheric imaging assembly (aia) on the solar dynamics observatory (sdo). *Solar Physics*, 275(1):17–40.

Leonard, A. and Morgan, H. (2014). Temperature diagnostics of the solar atmosphere using SunPy. *ArXiv e-prints*.

Li, J. (2011). Active longitudes revealed by large-scale and long-lived coronal streamers. *The Astrophysical Journal*, 735(2):130.

Madjarska, M. S. (2011). Dynamics and plasma properties of an X-ray jet from SUMER, EIS, XRT, and EUVI A B simultaneous observations. , 526:A19.

Mariska, J. T. (1986). The quiet solar transition region. , 24:23–48.

Martínez-Sykora, J., Hansteen, V., and Moreno-Insertis, F. (2011). On the Origin of the Type II Spicules: Dynamic Three-dimensional MHD Simulations. , 736:9.

Moe, O. K., Beckers, J. M., and Engvold, O. (1975). A comparison of spicules in the H-alpha and He II /304 A/ lines. , 40:65–68.

Moore, R. L., Cirtain, J. W., Sterling, A. C., and Falconer, D. A. (2010). Dichotomy of solar coronal jets: Standard jets and blowout jets. *The Astrophysical Journal*, 720(1):757.

Moore, R. L., Sterling, A. C., Cirtain, J. W., and Falconer, D. A. (2011). Solar X-ray Jets, Type-II Spicules, Granule-size Emerging Bipoles, and the Genesis of the Heliosphere. , 731:L18.

Moore, R. L., Tang, F., Bohlin, J. D., and Golub, L. (1977). H-alpha macrospicules - Identification with EUV macrospicules and with flares in X-ray bright points. , 218:286–290.

Moreno-Insertis, F., Galsgaard, K., and Ugarte-Urra, I. (2008). Jets in Coronal Holes: Hinode Observations and Three-dimensional Computer Modeling. , 673:L211.

Morton, R. J. (2012). Chromospheric jets around the edges of sunspots. , 543:A6.

Moschou, S. P., Tsinganos, K., Vourlidas, A., and Archontis, V. (2013). SDO Observations of Solar Jets. , 284:427–438.

Murawski, K., Srivastava, A. K., and Zaqarashvili, T. V. (2011). Numerical simulations of solar macrospicules. , 535:A58.

Mursula, K. and Hiltula, T. (2004). Systematically Asymmetric Heliospheric Magnetic Field: Evidence for a Quadrupole Mode and Non-Axisymmetry with Polarity Flip-Flops. , 224:133–143.

Narang, N., Arbacher, R. T., Tian, H., Banerjee, D., Cranmer, S. R., DeLuca, E. E., and McKillop, S. (2016). Statistical study of network jets observed in the solar transition region: a comparison between coronal holes and quiet-sun regions. *Solar Physics*, 291(4):1129–1142.

Nishizuka, N., Nakamura, T., Kawate, T., Singh, K. A. P., and Shibata, K. (2011). Statistical Study of Chromospheric Anemone Jets Observed with Hinode/SOT. , 731:43.

Obridko, V. N. and Shelting, B. D. (2007). Occurrence of the 1.3-year periodicity in the large-scale solar magnetic field for 8 solar cycles. *Advances in Space Research*, 40:1006–1014.

Parenti, S., Bromage, B. J. I., and Bromage, G. E. (2002). An erupting macrospicule. Characteristics derived from SOHO-CDS spectroscopic observations. , 384:303–316.

Patsourakos, S., Vial, J.-C., Gabriel, A. H., and Bellamine, N. (1999). Transition-Region Network Boundaries in the Quiet Sun: Width Variation with Temperature as Observed with CDS on SOHO. , 522:540–546.

Pereira, T. M. D., De Pontieu, B., and Carlsson, M. (2012). Quantifying Spicules. , 759:18.

Pereira, T. M. D., De Pontieu, B., Carlsson, M., Hansteen, V., Tarbell, T. D., Lemen, J., Title, A., Boerner, P., Hurlburt, N., Wülser, J. P., Martínez-Sykora, J., Kleint, L., Golub, L., McKillop, S., Reeves, K. K., Saar, S., Testa, P., Tian, H., Jaeggli, S., and Kankelborg, C. (2014). An Interface Region Imaging Spectrograph First View on Solar Spicules. , 792:L15.

Pesnell, W. D., Thompson, B. J., and Chamberlin, P. C. (2012). The Solar Dynamics Observatory (SDO). , 275:3–15.

Pike, C. D. and Harrison, R. A. (1997). Euv observations of a macrospicule: Evidence for solar wind acceleration? *Solar Physics*, 175(2):457–465.

Pike, C. D. and Mason, H. E. (1998). Rotating Transition Region Features Observed with the SOHO Coronal Diagnostic Spectrometer. , 182:333–348.

Priest, E. and Forbes, T. (2007). *Magnetic Reconnection*.

Reale, F. (2014). Coronal Loops: Observations and Modeling of Confined Plasma. *Living Reviews in Solar Physics*, 11.

Richey, M. (2010). The evolution of markov chain monte carlo methods. *The American Mathematical Monthly*, 117(5):383–413.

Rouppe van der Voort, L. and de la Cruz Rodríguez, J. (2013). Short Dynamic Fibrils in Sunspot Chromospheres. , 776:56.

Rouppe van der Voort, L., De Pontieu, B., Pereira, T. M. D., Carlsson, M., and Hansteen, V. (2015). Heating Signatures in the Disk Counterparts of Solar Spicules in Interface Region Imaging Spectrograph Observations. , 799:L3.

Rouppe van der Voort, L., Leenaarts, J., de Pontieu, B., Carlsson, M., and Vissers, G. (2009). On-disk Counterparts of Type II Spicules in the Ca II 854.2 nm and Hα Lines. , 705:272–284.

Russell, H. N. (1914). Relations Between the Spectra and Other Characteristics of the Stars. *Popular Astronomy*, 22:275–294.

Scharmer, G. B., Bjelksjo, K., Korhonen, T. K., Lindberg, B., and Petterson, B. (2003). The 1-meter Swedish solar telescope. In Keil, S. L. and Avakyan, S. V., editors, *Innovative Telescopes and Instrumentation for Solar Astrophysics*, volume 4853 of , pages 341–350.

Schmelz, J. T., Jenkins, B. S., and Kimble, J. A. (2013). Atmospheric Imaging Assembly Response Functions: Solving the Fe viii Problems with Hinode EIS Bright Point Data. , 283:325–340.

Scullion, E., Doyle, J. G., and Erdélyi, R. (2010). A spectroscopic analysis of macrospicules . , 81:737.

Scullion, E., Popescu, M. D., Banerjee, D., Doyle, J. G., and Erdélyi, R. (2009). Jets in Polar Coronal Holes. , 704:1385–1395.

Sekse, D. H., Rouppe van der Voort, L., De Pontieu, B., and Scullion, E. (2013). Interplay of Three Kinds of Motion in the Disk Counterpart of Type II Spicules: Upflow, Transversal, and Torsional Motions. , 769:44.

Shibata, K., Ishido, Y., Acton, L. W., Strong, K. T., Hirayama, T., Uchida, Y., McAllister, A. H., Matsumoto, R., Tsuneta, S., Shimizu, T., Hara, H., Sakurai, T., Ichimoto, K., Nishino, Y., and Ogawara, Y. (1992). Observations of X-ray jets with the YOHKOH Soft X-ray Telescope. , 44:L173–L179.

Shibata, K. and Suematsu, Y. (1982). Why are spicules absent over plages and long under coronal holes. , 78:333–345.

Shibata, K. and Uchida, Y. (1986). Sweeping-magnetic-twist mechanism for the acceleration of jets in the solar atmosphere. , 103:299–310.

Shimojo, M., Hashimoto, S., Shibata, K., Hirayama, T., Hudson, H. S., and Acton, L. W. (1996). Statistical Study of Solar X-Ray Jets Observed with the YOHKOH Soft X-Ray Telescope. , 48:123–136.

St. Cyr, O. C., Sánchez-Duarte, L., Martens, P. C. H., Gurman, J. B., and Larduinat, E. (1995). SOHO Ground Segment, Science Operations, and Data Products. , 162:39–59.

Sterling, A. C. (2000). Solar Spicules: A Review of Recent Models and Targets for Future Observations - (Invited Review). , 196:79–111.

SunPy Community, T., Mumford, S. J., Christe, S., Pérez-Suárez, D., Ireland, J., Shih, A. Y., Inglis, A. R., Liedtke, S., Hewett, R. J., Mayer, F., Hughitt, K., Freij, N., Meszaros, T., Bennett, S. M., Malocha, M., Evans, J., Agrawal, A., Leonard, A. J., Robitaille, T. P., Mampaey, B., Iván Campos-Rozo, J., and Kirk, M. S. (2015). SunPyPython for solar physics. *Computational Science and Discovery*, 8(1):014009.

Takeuchi, A. and Shibata, K. (2001). Magnetic Reconnection Induced by Convective Intensification of Solar Photospheric Magnetic Fields. , 546:L73–L76.

Tian, H., DeLuca, E. E., Cranmer, S. R., De Pontieu, B., Peter, H., Martínez-Sykora, J., Golub, L., McKillop, S., Reeves, K. K., Miralles, M. P., McCauley, P., Saar, S., Testa, P., Weber, M., Murphy, N., Lemen, J., Title, A., Boerner, P., Hurlburt, N., Tarbell, T. D., Wuelser, J. P., Kleint, L., Kankelborg, C., Jaeggli, S., Carlsson, M., Hansteen, V., and McIntosh, S. W. (2014). Prevalence of small-scale jets from the networks of the solar transition region and chromosphere. *Science*, 346(27):1255711.

Tsiropoula, G., Tziotziou, K., Kontogiannis, I., Madjarska, M. S., Doyle, J. G., and Suematsu, Y. (2012). Solar Fine-Scale Structures. I. Spicules and Other Small-Scale, Jet-Like Events at the Chromospheric Level: Observations and Physical Parameters. , 169:181–244.

Tsuneta, S., Acton, L., Bruner, M., Lemen, J., Brown, W., Caravalho, R., Catura, R., Freeland, S., Jurcevich, B., Morrison, M., Ogawara, Y., Hirayama, T., and Owens, J. (1991). The Soft X-ray Telescope for the SOLAR-A Mission. , 136:37–67.

Ulmschneider, P. and Stein, R. F. (1982). Heating of stellar chromospheres when magnetic fields are present. , 106:9–13.

Usoskin, I. G., Berdyugina, S. V., and Poutanen, J. (2005). Preferred sunspot longitudes: non-axisymmetry and differential rotation. , 441:347–352.

van Noort, M., Rouppe van der Voort, L., and Löfdahl, M. G. (2005). Solar Image Restoration By Use Of Multi-frame Blind De-convolution With Multiple Objects And Phase Diversity. , 228:191–215.

Vernazza, J. E., Avrett, E. H., and Loeser, R. (1981). Structure of the solar chromosphere. III - Models of the EUV brightness components of the quiet-sun. , 45:635–725.

Vourlidas, A. (2006). A Review of White Light Streamers at the End of Cycle 23. In Bothmer, V. and Hady, A. A., editors, *Solar Activity and its Magnetic Origin*, volume 233 of *IAU Symposium*, pages 197–204.

Wang, H. (1998). Comparison of Hα and He II λ304 Macrospicules. , 509:461–470.

Wilkinson, L. K. (1991). The Distribution of Longitudinal Currents in Sunspots. In *Bulletin of the American Astronomical Society*, volume 23 of , page 1030.

Withbroe, G. L., Jaffe, D. T., Foukal, P. V., Huber, M. C. E., Noyes, R. W., Reeves, E. M., Schmahl, E. J., Timothy, J. G., and Vernazza, J. E. (1976). Extreme-ultraviolet transients observed at the solar pole. , 203:528–532.

Withbroe, G. L. and Noyes, R. W. (1977). Mass and energy flow in the solar chromosphere and corona. , 15:363–387.

Woeger, F. (2016). The DKIST Instrumentation Suite. In *AAS/Solar Physics Division Meeting*, volume 47 of *AAS/Solar Physics Division Meeting*, page 201.02.

Xia, L. D., Popescu, M. D., Doyle, J. G., and Giannikakis, J. (2005). Time series study of euv spicules observed by sumer/soho. *A&A*, 438(3):1115–1122.

Yamauchi, Y., Moore, R. L., Suess, S. T., Wang, H., and Sakurai, T. (2004). Macrospicules, Coronal Heating, and SolarB. In Sakurai, T. and Sekii, T., editors, *The Solar-B Mission and the Forefront of Solar Physics*, volume 325 of *Astronomical Society of the Pacific Conference Series*, page 301.

Zaqarashvili, T. V. and Erdélyi, R. (2009). Oscillations and Waves in Solar Spicules. , 149:355–388.

Zaqarashvili, T. V., Vörös, Z., and Zhelyazkov, I. (2014). Kelvin-Helmholtz instability of twisted magnetic flux tubes in the solar wind. , 561:A62.

Zhang, L. Y., Wang, H. N., Du, Z. L., Cui, Y. M., and He, H. (2007). Long-term behavior of active longitudes for solar X-ray flares. , 471:711–716.

Zhang, Y. Z., Shibata, K., Wang, J. X., Mao, X. J., Matsumoto, T., Liu, Y., and Su, J. T. (2012). Revision of Solar Spicule Classification. , 750:16.

Åke Nordlund, Stein, R. F., and Asplund, M. (2009). Solar surface convection. *Living Reviews in Solar Physics*, 6(2).